

NASA CR-132518

STUDY OF THE USE OF METAL-OXIDE-SILICON (MOS) DEVICES
FOR PARTICULATE DETECTION AND MONITORING
IN THE EARTH'S ATMOSPHERE

by

A. D. Brooks
L. K. Monteith
J. J. Wortman
J. C. Mulligan

Prepared under Contract No. NAS1-12714

Research Triangle Institute
Research Triangle Park, N.C.

for

Langley Research Center
National Aeronautics and Space Administration

RTI Project 43U-929

November 1974

PREFACE

N 75 - 11446

This report describes investigations by the Research Triangle Institute, Research Triangle Park, North Carolina on NASA Contract NAS1-12714, "Study of the Use of Metal-Oxide-Silicon (MOS) Devices for Particulate Detection and Monitoring in the Earth's Atmosphere." This study was monitored by Mr. Robert L. O'Neal of Langley Research Center.

The study was performed in the Engineering Division of the Research Triangle Institute with Mr. A. D. Brooks as Project Leader. Dr. J. J. Wortman of the Institute and Drs. L. K. Monteith and J. C. Mulligan of North Carolina State University made major contributions to the study.

We also wish to acknowledge our appreciation for the technical advice and loan of some equipment from the Environmental Protection Agency.

ABSTRACT

A metal-oxide-silicon (MOS) capacitor-type particulate sensor was evaluated for use in atmospheric measurements. An accelerator system was designed and tested for the purpose of providing the necessary energy to trigger the MOS-type sensor. The accelerator system and the MOS sensor were characterized as a function of particle size and velocity. Diamond particles were used as particulate sources in laboratory tests.

Preliminary tests were performed in which the detector was mounted on an aircraft and flown in the vicinity of coal-fired electric generating plants.

STUDY OF THE USE OF METAL-OXIDE-SILICON (MOS) DEVICES
FOR PARTICULATE DETECTION AND MONITORING
IN THE EARTH'S ATMOSPHERE

Table of Contents

Preface	ii
Abstract	iii
List of Figures	v
List of Tables	vii
1.0 INTRODUCTION	1
2.0 CALIBRATION PARTICLE SELECTION	3
2.1 PARTICLE DISPERSION METHOD	3
2.2 PARTICLE SUSPENSION PREPARATION	7
3.0 DIAMOND PARTICLE DISTRIBUTION SYSTEM	10
4.0 CLIMET PARTICLE COUNTER	12
5.0 MOS SENSOR FABRICATION	16
6.0 VACUUM NOZZLE PARTICLE ACCELERATOR	20
7.0 MOS ELECTRONICS	24
8.0 DATA-GATHERING METHODS	28
8.1 THRESHOLD DATA	30
8.2 VARIABLE BIAS DATA	34
8.3 VARIABLE PRESSURE DATA	34
8.4 IN-FLIGHT SENSOR EVALUATION	38
9.0 ANALYSIS	44
10.0 DISCUSSION	50
11.0 APPLICATION	56
APPENDIX A: Gas and Particle Flow Characteristics for Suction Type Particle Accelerator used with MOS Detector	58

List of Figures

1	Size Distribution of 1- μ Diamond Particles	4
2	Size Distribution of 3- μ Diamond Particles	5
3	Size Distribution of 6- μ Diamond Particles	6
4	Schematic Representation of Particle Distribution System	11
5	Photograph of the Climet Particle Counter	14
6	Block Diagram of the Climet Particle Counter	15
7	Cross Section of MOS sensor	17
8	Photomicrograph of MOS Sensor	19
9	Modified Vacuum Nozzle Particle Accelerator	21
10	Photograph of Vacuum Nozzle Particle Accelerator	22
11	Sampling Characteristics of Vacuum Nozzle Particle Accelerator	23
12	MOS Discharge Pulse	25
13	Schematic Diagram of the MOS Readout Circuit	26
14	A Schematic Representation of the Calibration System	29
15	Particle Velocity as a Function of Particle Accelerator Nozzle Pressure (3 μ , 9 μ , and 15 μ Diameter Particles)	31
16	Particle Diameter-Mass for Diamond Microparticles	32
17	Particle Mass-Velocity Threshold for Initiating MOS Capacitor Discharge	33
18	Dependence of Velocity Threshold on Applied Voltage	35
19	MOS Counting Efficiency Relative to Climet 6-Micron Particle Distribution (1200 Å SiO ₂)	36
20	Photomicrograph of Impacted MOS Sensor	37
21	Illustration of Geometrical Considerations to Determine Counting Efficiency	39
22	Schematic of MOS Sensor Counting Circuit Used in Flight Evaluation	40

List of Figures (Continued)

23	Block Diagram of MOS Sensor Counting System	40
24	Photograph of MOS Sensor on Wing Spar of Aircraft	43
25	Illustration of the Particle Penetration Geometry	46
A-1	Nozzle Flow and Velocity versus Nozzle Pressure	67
A-2	Nozzle and Straight Tube Combination	69
A-3	Particle Velocities as Functions of Nozzle Pressure	76

List of Tables

1	Particle Counting Statistics and Accuracy of Climet	13
2	Particle Penetration Threshold for Various Silicon Oxide Thicknesses with Electric Field of 2.2×10^6 volts/cm	48

1.0 INTRODUCTION

The primary objective of this research effort was to construct, test, and calibrate a sensor to count microparticles from roughly 1 to 10 microns. Typical applications were considered to be the sensing of particulate matter from solid propellant rocket exhausts (alumina), particulate matter in the upper atmosphere of concern from supersonic transports, and emissions from stationary sources such as power plants and from dusty environments such as rock quarries and coal mines.

The microparticle sensor is a capacitor-type sensor where the impacting particle initiates a temporary short through the dielectric of the capacitor. The large current density through the shorted region of the capacitor raises the temperature in the region about the impact so that the material (dielectric, particle, electrode) in this region is vaporized. With the short circuit removed, the capacitor recharges. From penetration theory one expects that the microparticles at subsonic velocities will cause a discharge upon penetration to some fraction of their diameters. To insure adequate penetration to initiate an electrical discharge, the dielectric of the capacitor was chosen as thin as practical with modern silicon-silicon oxide technology. Silicon technology was chosen due to the sophistication and understanding available to achieve a very thin, reliable, and reproducible dielectric. Typically, the final capacitor is approximately 1000 \AA , thermally grown silicon oxide film on low resistivity (less than 1 ohm-cm) silicon wafer with a 500 \AA aluminum electrode which is impacted by the microparticle.

The major problems encountered during this research effort were (1) obtaining a well-defined and reproducible particle source, (2) reducing

unwanted and random sources of particles from the system, and (3) accelerating particles to a velocity necessary to initiate a discharge. Much of the early effort was devoted to development of particle selection techniques. Well-defined polystyrene microparticles and organic particles were used; however, they would not initiate a reliable discharge. Our experience has shown that either density or hardness near that for alumina and diamond will initiate discharges. However, the major effort and probably the most significant result is the design of a microparticle dispensing system which provides a range of small particles with a degree of reproducibility unobtainable prior to this effort. Only through detailed design and analysis could the influence of factors such as unwanted microparticles throughout the system be identified.

Finally, it should be pointed out that the sensor designed and tested in this research effort will count microparticles with a diameter greater than 2 microns and a density near 3.5 gm/cm^3 . The capacitor-type units were compared with a commercially available unit for counting microparticles, and the counts compared favorably and well within experimental error.

2.0 CALIBRATION PARTICLE SELECTION

Diamond particles were chosen for the calibration source mainly for two reasons: (1) their hardness properties and (2) their narrow size distribution. Through previous experience with polystyrene, organic crystals, and alumina microparticles, the hardness of the particle is an important factor in obtaining reliable discharges of the impacted MOS capacitor. The narrow size distribution property was important in order to obtain a meaningful calibration of the MOS sensors for different size particles.

The diamond particles were obtained from the Geoscience Instruments Corporation and were purchased in the following size ranges: 0.25 μ , 1.0 μ , 3.0 μ , 6.0 μ , 9.0 μ , and 15.0 μ . Shown below is a size distribution table for these particles.

Average size	0.25 μ	1 μ	3 μ	6 μ	9 μ	15 μ
Distribution	(0.1-5)	(0.5-2)	(2-4)	(4-8)	(8-12)	(12-20)

Also shown in Figures 1, 2, and 3 are distribution curves for the 1 μ , 3 μ , and 6 μ particles, respectively.

2.1 PARTICLE DISPERSION METHOD

The method chosen for dispersion of the diamond particles was to suspend the particles in isopropyl alcohol and to spray them into a sampling chamber with an atomizer. The suspension method was chosen because of the difficulty encountered in dispersing dry particles due to coagulation. Also, this method allowed much more accurate control of the number and uniformity of the dispersed particles.

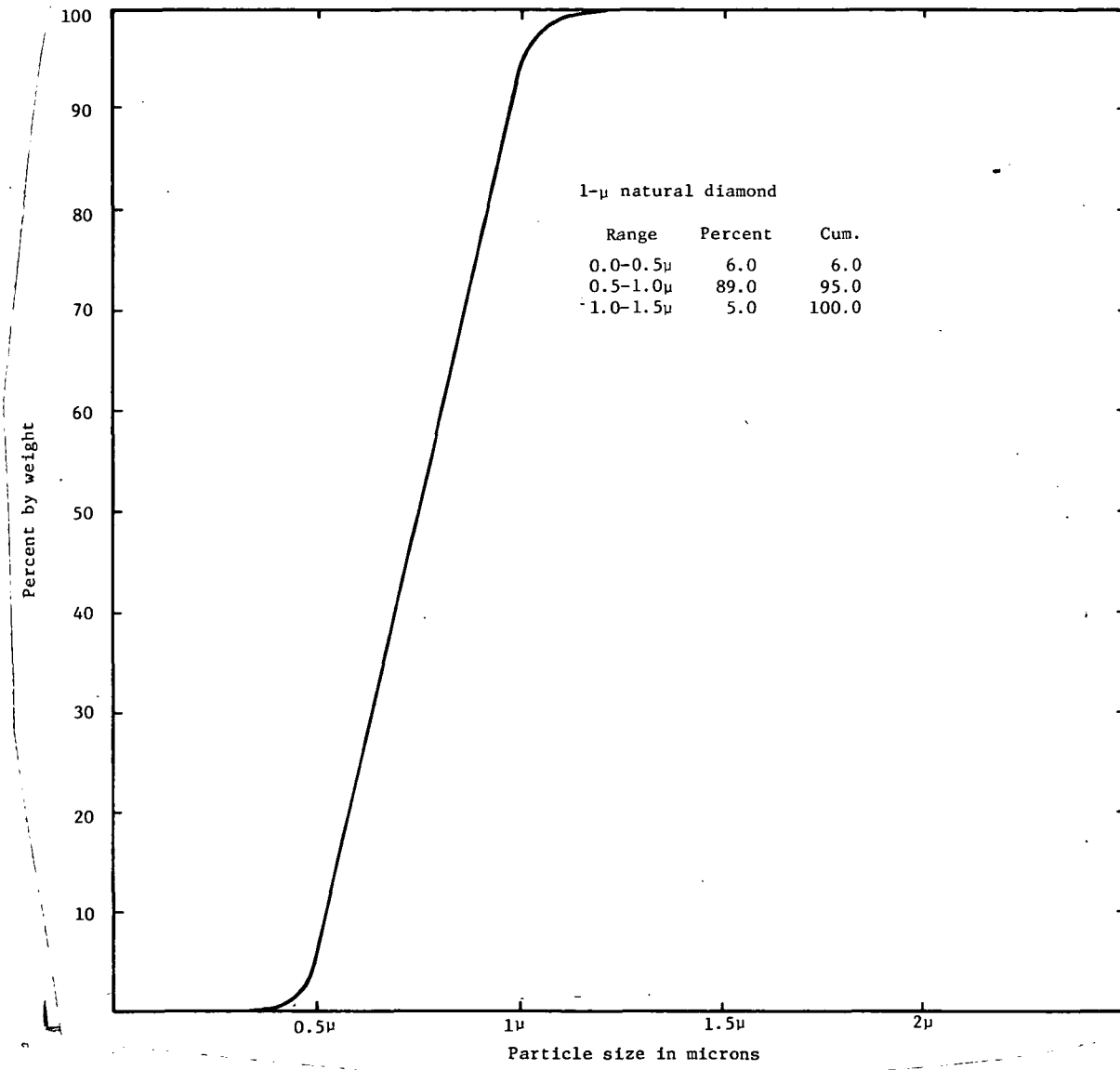


Figure 1. Size Distribution of 1- μ Diamond Particles.

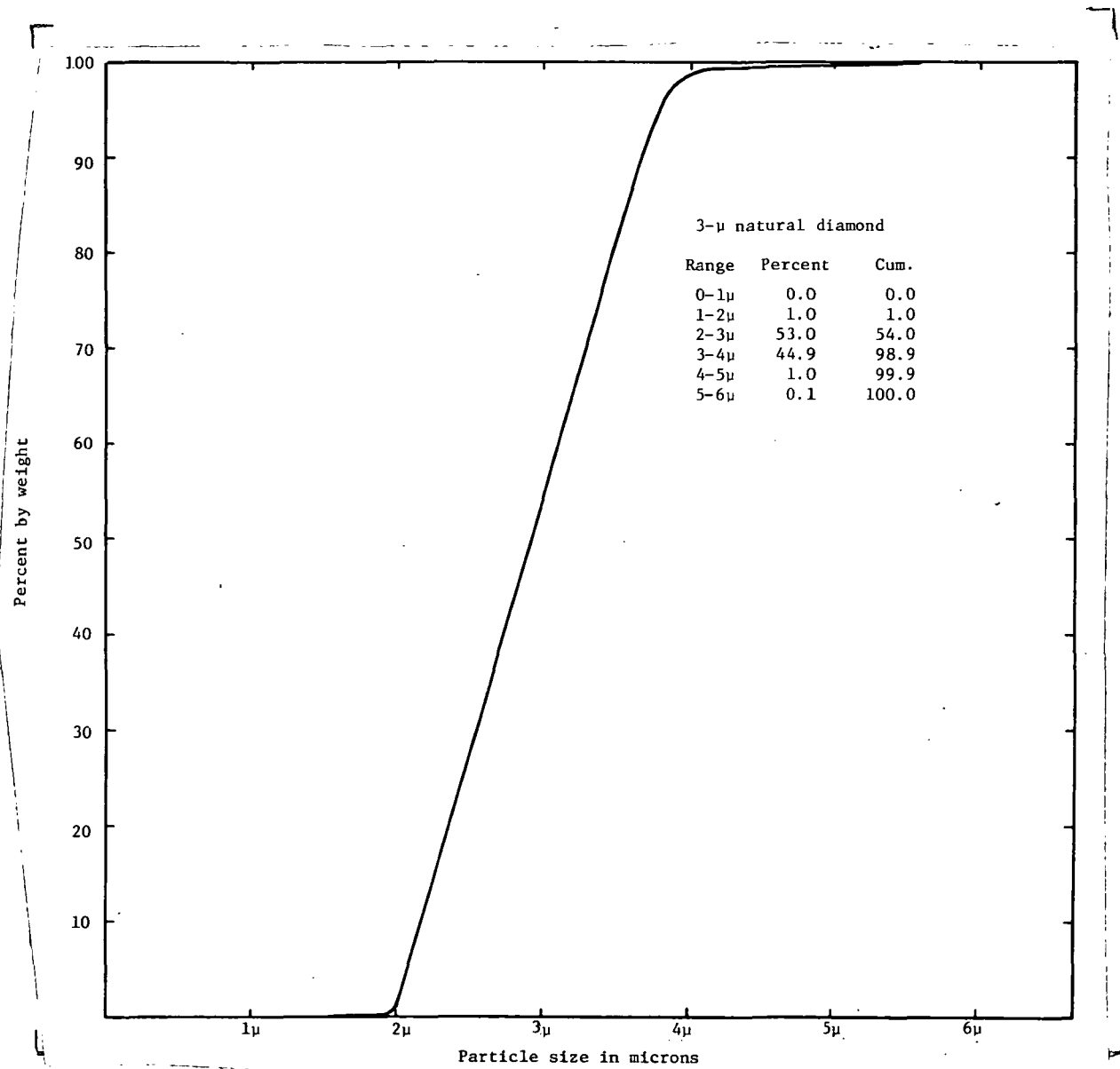


Figure 2. Size Distribution of 3- μ Diamond Particles.

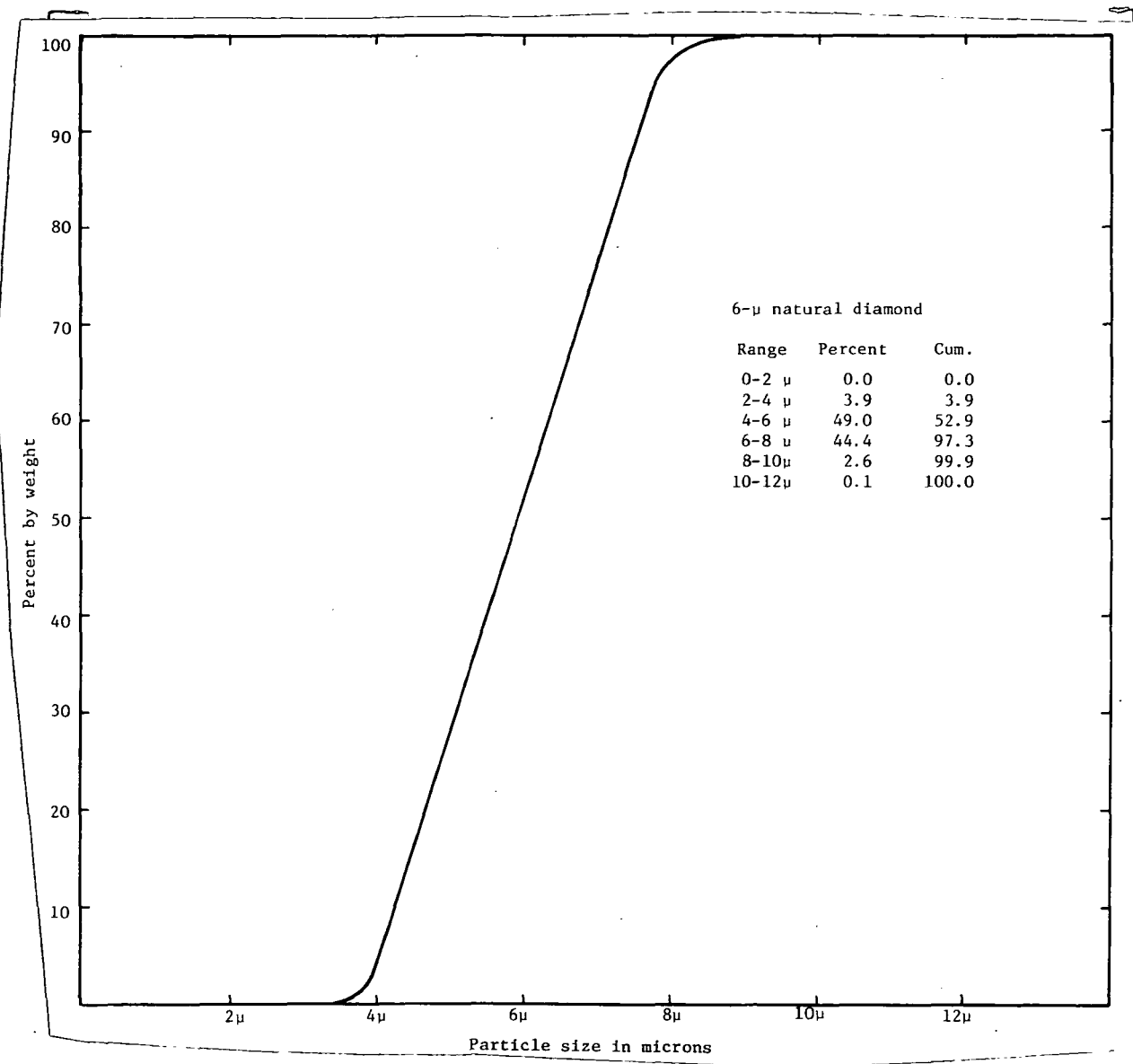


Figure 3. Size Distribution of 6- μ Diamond Particles.

2.2 PARTICLE SUSPENSION PREPARATION

Isopropyl alcohol was used for the suspension fluid because it is a volatile fluid with a comparatively high viscosity. As a first step in preparing the diamond particle suspension fluid, a particle background level in the isopropyl alcohol was determined by spraying the fluid into a sampling chamber with an atomizer driven by filtered nitrogen and sampling with a Climet Model 250 particle counter.

Although the particle size distribution was very narrow, a sizeable number of smaller than nominal size particles in a given range were present. The method used for separating these smaller particles from the particles in the size range of interest was as follows. The settling velocity in isopropyl alcohol was calculated for the particles in the size range of interest. The particles were weighed out and placed in a glass container with a known volume of isopropyl alcohol. These were thoroughly mixed until they were uniformly distributed in the solution. The time for the particles of interest to settle to the bottom of the container was determined using the height of the saturated fluid in the container and the calculated settling velocity of these particles. After the particles of interest had settled to the bottom of the container, the fluid containing the still suspended smaller particles was carefully siphoned into a graduated cylinder. This volume of fluid (isopropyl alcohol) was replaced by clean fluid. This procedure was repeated once in the case of the 6 μ and 9 μ particles and twice for the 3 μ particles. This was necessary in order to obtain a solution of particles which would contain mainly the particles in the size range of interest. Shown below is the method used for determining the settling velocity and the settling time for the particles of interest. Also shown is a table containing the calculated settling

velocities of various sized diamond particles in isopropyl alcohol. The settling velocity, v_s , is given by

$$v_s = \frac{\rho g d^2}{18n}$$

where ρ = density of particle

g = acceleration due to gravity

d = diameter of particle

n = viscosity of suspension fluid.

In air, 1- μ spherical particles of unit density have a settling velocity

$$v_s = 3.49 \times 10^{-3} \text{ cm/sec.}$$

In isopropyl alcohol, the settling velocity of the diamond particles may be obtained by introducing the ratio of the viscosity of isopropyl alcohol to air and the particle density where

$$\frac{\text{Viscosity of isopropyl}}{\text{Viscosity of air}} = \frac{2 \times 10^{-2} \text{ poise}}{1.82 \times 10^{-4} \text{ poise}} = 1.099 \times 10^{-2}$$

and

$$\text{Density of diamond} = 3.5,$$

yielding

$$v_s = \frac{(3.5)(d^2)(3.49 \times 10^{-3} \text{ cm/sec})(60 \text{ sec/min})}{1.099 \times 10^{-2}}$$

$$= (d^2) 6.67 \times 10^{-3} \text{ cm/min.}$$

Particle size (μ)	0.5 μ	1 μ	3 μ	6 μ	9 μ	15 μ
v_s (cm/min)	0.0016	0.0066	0.06	0.24	0.54	1.5

Settling time = $\frac{\text{height of fluid (cm)}}{v_s}$.

3.0 DIAMOND PARTICLE DISTRIBUTION SYSTEM

Due to the more rapid settling velocity and aerodynamic properties of the diamond particles, the Environmental Research Corporation fluid atomization generator, originally planned to be used to disperse the particles, would not efficiently disperse the large particles. Because of this, a particle dispersing system was designed which overcame these problems and would dispense the large diamond particles. An illustration of this system is shown in Figure 4. The isopropyl alcohol solution containing the suspended diamond particles is stirred by a magnetic stirrer to maintain a uniform suspension of particles and is then fed by a combination of gravity and venturi action to the nozzle in the sampling chamber. By using the gravity feed technique, one is assured of getting the large particles into the chamber. The venturi-type atomization nozzle was fed by nitrogen filtered by a $0.45-\mu$ filter at 30 psi. The nitrogen flow rate through the nozzle was measured by a wet test meter to be 21 liters/minute. The high velocity stream of nitrogen through the venturi nozzle caused the isopropyl alcohol solution containing the suspended diamond particles to be sprayed into the chamber in a fine mist. The alcohol evaporated before striking the opposite wall of the sampling chamber, allowing the particles to settle by gravitational action to the bottom of the sampling chamber where they were simultaneously sampled by the Climet Model 250 particle counter and the MOS vacuum nozzle particle accelerator. An additional $0.45-\mu$ filtered nitrogen source of 18 liters/minute was added to the chamber so that the total nitrogen input was approximately a factor of two greater than the combined sampling rates of the Climet and the vacuum nozzle particle accelerator. This technique insures that a slight positive pressure remains in the sampling chamber, thus eliminating any effect from the surrounding atmosphere.

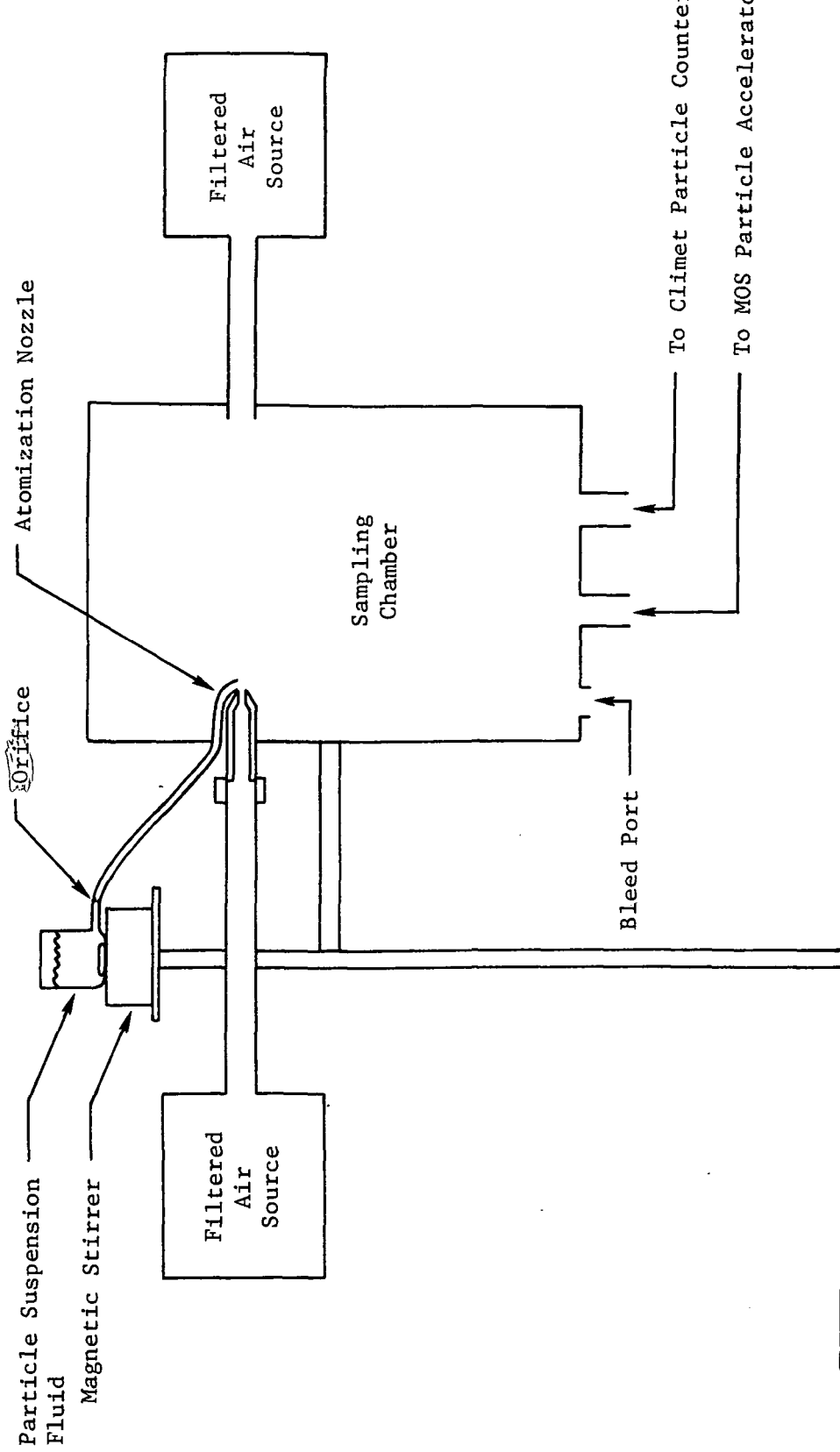


Figure 4. Schematic Representation of Particle Distribution System

4.0 CLIMET PARTICLE COUNTER

The Climet Model CI-250 particle counter was used as a reference during the calibration of the MOS particulate sensors. The Climet particle counter is a portable, solid-state, optical instrument operating on the light-scattering principle. The air or gas containing the particles to be sampled is pulled into the instrument by a vacuum pump at a rate of 14 ft³/hr. The large sampling rate is to insure that all the particles in the sample will enter the instrument. The sampling air stream is divided so that 1 ft³/hr of the sample is pulled through the optical counting chamber. Any particle which enters the counting chamber causes the light to be scattered. The scattered light pulse, which has an amplitude proportional to the size of the particle, passes through a lens system and strikes a silicon photocell. The electrical pulse from the photocell is fed to a comparator circuit which is controlled by the particle size range switch on the instrument. Any particles which are equal to or larger than the particle size range switch setting produce pulses which trigger the comparator circuit which in turn drives the digital counter. The counting time is controlled by selecting a 36-second, a 360-second, or a manual mode of operation. The accuracy of the instrument is illustrated in Table 1. A picture of the instrument and a block diagram are shown in Figures 5 and 6, respectively.

The instrument was modified for use in this study. It was found that the large particles (75 μ) would not reach the counting chamber through the normal plumbing. A plastic pipe was inserted directly into the chamber and positioned in a vertical manner so that particles would fall directly from the source to the chamber.

Table 1. Particle Counting Statistics and Accuracy of Climet

Number of particles counted	Percent error			Standard deviation of counts, δ
	50% probability	95% probability	99.7% probability	
99,999	± 0.213	± 0.63	± 0.95	316
10,000	± 0.67	± 2.0	± 3.0	100
1,000	± 2.13	± 6.3	± 9.5	31.6
100	± 6.7	± 20	± 30	10
10	± 21.5	+65 -60	+100 -75	3.16
1	+200 - 70	+300 - 90	+500 -100	1



Figure 5. Photograph of the Climet Particle Counter.

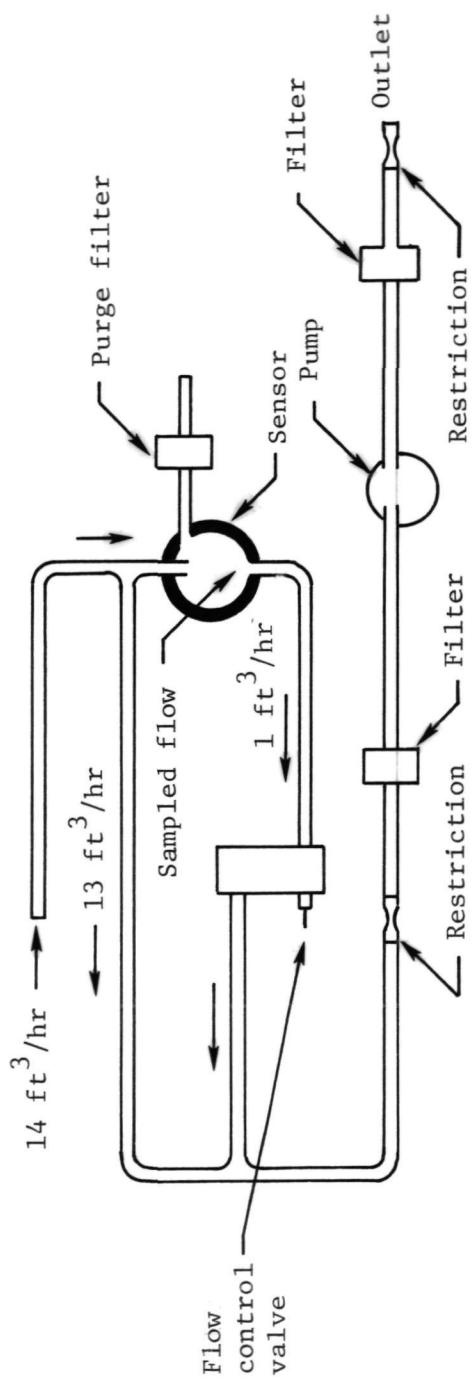


Figure 6. Block Diagram of the Climet Particle Counter.

5.0 MOS SENSOR FABRICATION

The MOS particle sensors are basically MOS capacitors fabricated by using standard integrated circuit processes. The basic structure of the MOS sensor is a silicon substrate acting as one "capacitor plate," a thermally grown SiO_2 layer acting as a dielectric, and an evaporated aluminum film acting as the second capacitor plate. A cross-section of the unit is shown in Figure 7. The silicon substrate material is p-type 0.1 $\mu\text{-cm}$, 1-1-1 oriented, 1-1/4-inch diameter wafers polished on one side. Following is a description of the MOS sensor fabrication process.

The first step in the fabrication process was to prepare the silicon substrate and grow the SiO_2 film. The silicon substrates were cleaned by employing standard silicon cleaning procedures which included heating the substrate in solvents and acids. The oxidation step was carried out by loading the substrates into a quartz oxidation tube of an oxidation furnace which was at 1100°C, with 2000 cc of dry O_2 flowing through it. The time of oxidation was varied in order to produce SiO_2 films of 700 $\overset{\circ}{\text{A}}$, 1000 $\overset{\circ}{\text{A}}$, 1200 $\overset{\circ}{\text{A}}$, 1500 $\overset{\circ}{\text{A}}$, and 1800 $\overset{\circ}{\text{A}}$.

The next step was to anneal the substrates containing the SiO_2 layers at 200°C in a vacuum of 25 in. Hg for 30 minutes. The wafers were then placed in the aluminum evaporation system on evaporation masks which contained a 50 \times 50 array of 15-mil diameter holes on 20-mil centers. A standard aluminum evaporation cycle was carried out which produced 500 $\overset{\circ}{\text{A}}$ thick, 15-mil diameter dots of aluminum on the SiO_2 surface.

The next step in the fabrication sequence was to etch the SiO_2 from the lapped back side of the wafer by positioning the wafers, aluminum side down, and placing crystals of ammonium bifluoride ($\text{NH}_4\text{F}\cdot\text{HF}$) on the

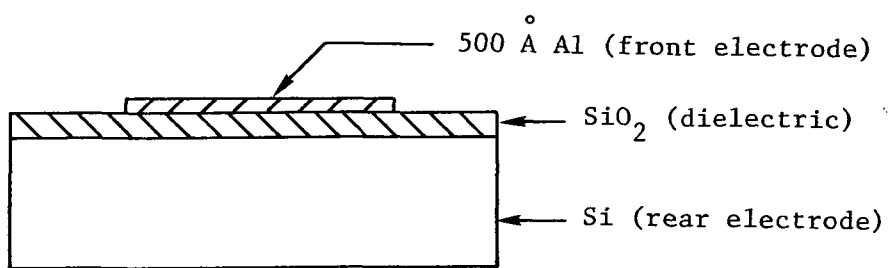


Figure 7. Cross Section of MOS Sensor.

lapped wafer surface. A few drops of D.I. H₂O were placed on the crystals, and when the SiO₂ was etched away, they were rinsed in D.I. H₂O.

The next step was to evaporate 500 Å of aluminum on the etched back surface of the silicon wafers. After this step, the silicon wafers were scribed into 100 × 100 mil square chips containing approximately a 5 × 5 array of 15-mil diameter dots. These 100-mil chips were eutectically bonded to 12 pin gold-plated TO-5 headers by scrubbing the chip in a random motion on the TO-5 header at 450°C. The eutectic bond formed was mechanically strong and produced a good electrical contact between the silicon chip and the TO-5 header.

The next step was to bond 1-mil gold leads from eleven of the 15-mil aluminum dots to the posts on the TO-5 header. The twelfth post was bonded to the base of the TO-5 header and served as a common contact for the eleven 15-mil diameter MOS capacitors. A photomicrograph of the completed MOS particle sensor is shown in Figure 8.

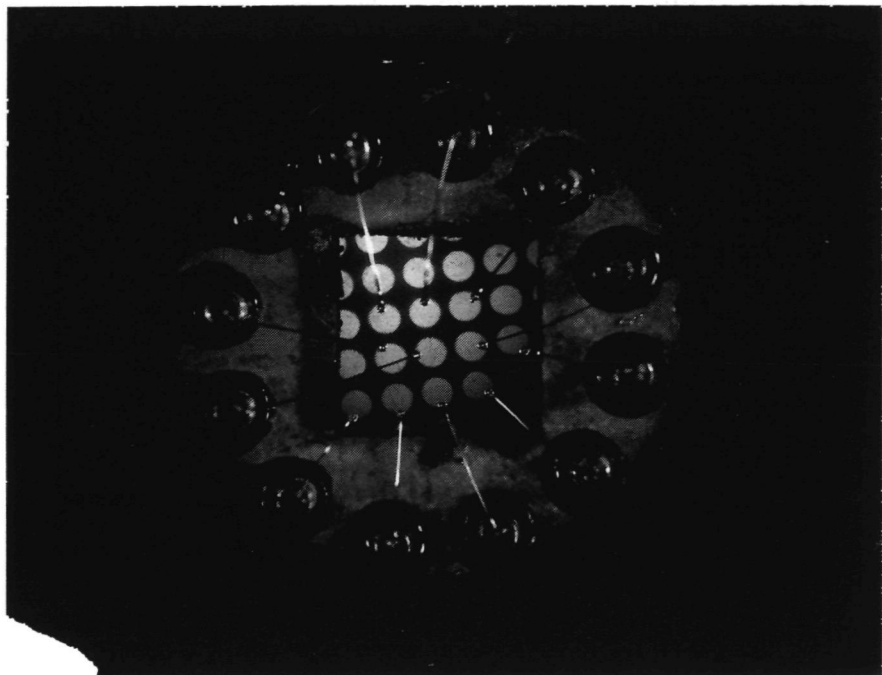


Figure 8. Photomicrograph of MOS Sensor.

6.0 VACUUM NOZZLE PARTICLE ACCELERATOR

The purpose of the vacuum nozzle particle accelerator is to accelerate the particles to a velocity sufficient to produce counting on the MOS particle sensor. A sketch and a photograph of the accelerator are shown in Figures 9 and 10, respectively. The vacuum nozzle particle accelerator was chosen, as a means of obtaining the necessary particle acceleration, because of its simplicity of design and compact size.

The design criteria are given in the Appendix. The particle acceleration tube was added to the vacuum nozzle particle accelerator in order to provide sufficient distance, and thus time, for the 6μ and larger diamond particles to reach a velocity sufficient to produce counting on the MOS sensor. The TO-5 MOS particle sensor was mounted into a standard 12-pin TO-5 I-C socket which positioned and aligned the sensor in front of the particle acceleration nozzle. The alignment of the MOS particle sensor was found to be a very important factor during the design of the vacuum nozzle particle sensor. The 0.5-inch nozzle-to-MOS sensor distance was chosen in order to prevent small, soft particles of insufficient mass from producing counts and from accumulating on the MOS sensor surface, thus lowering the counting efficiency of the sensor. In operation, a vacuum pump was connected to the vacuum port on the vacuum nozzle particle accelerator, and the vacuum nozzle pressure was measured at the vacuum port. A plot of the sampling rate versus the vacuum nozzle pressure is shown in Figure 11.

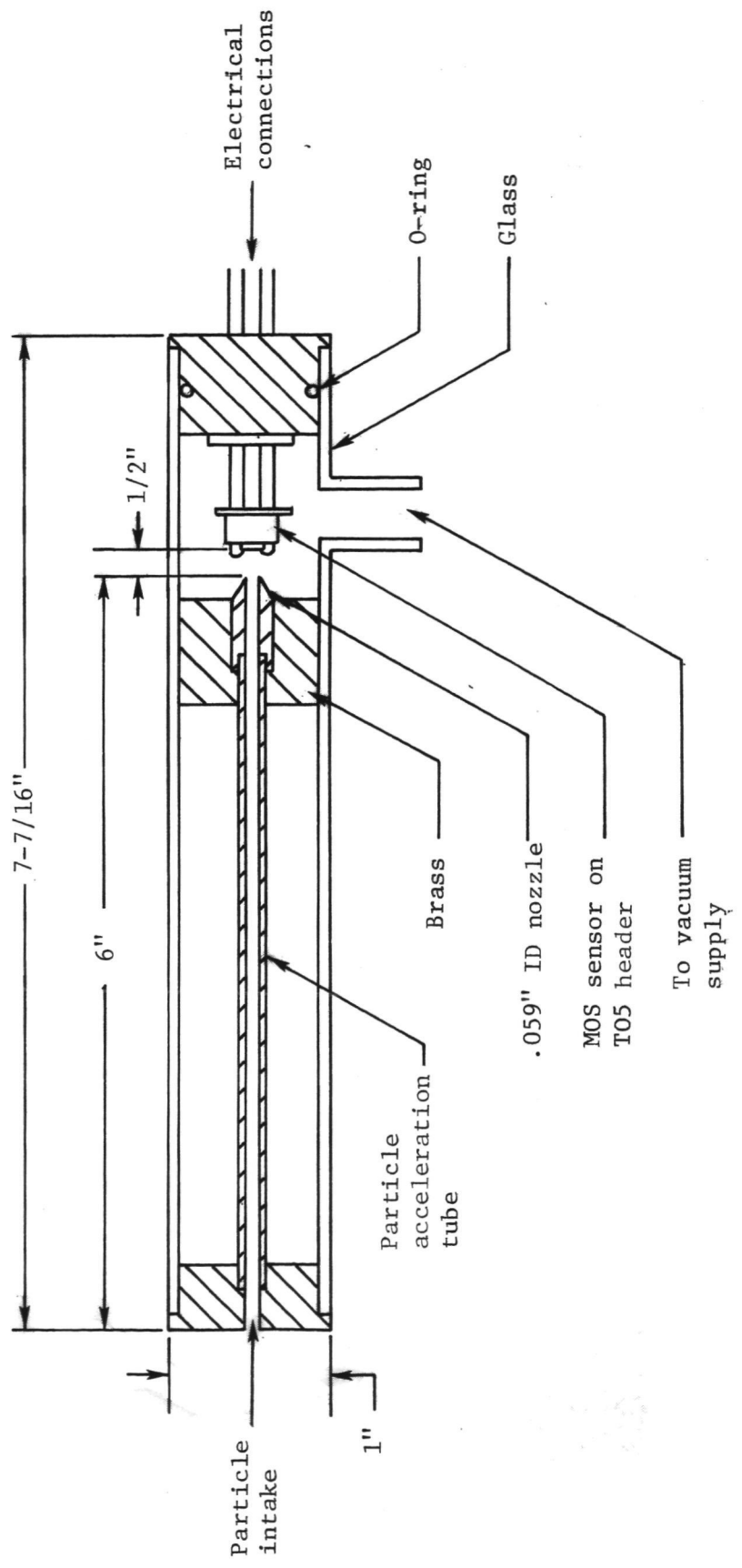


Figure 9. Modified Vacuum Nozzle Particle Accelerator.

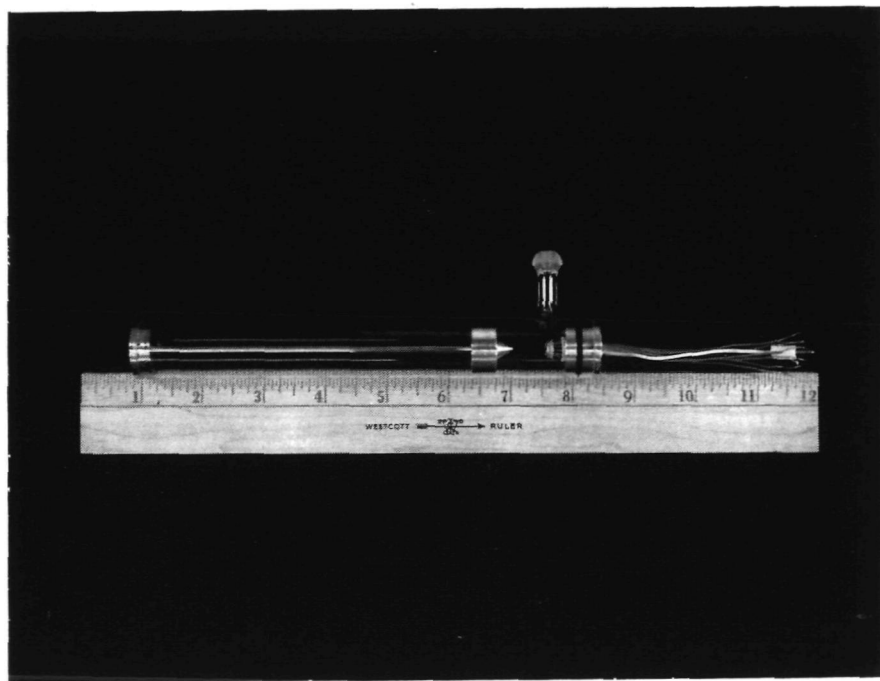


Figure 10. Photograph of Vacuum Nozzle Particle Accelerator.

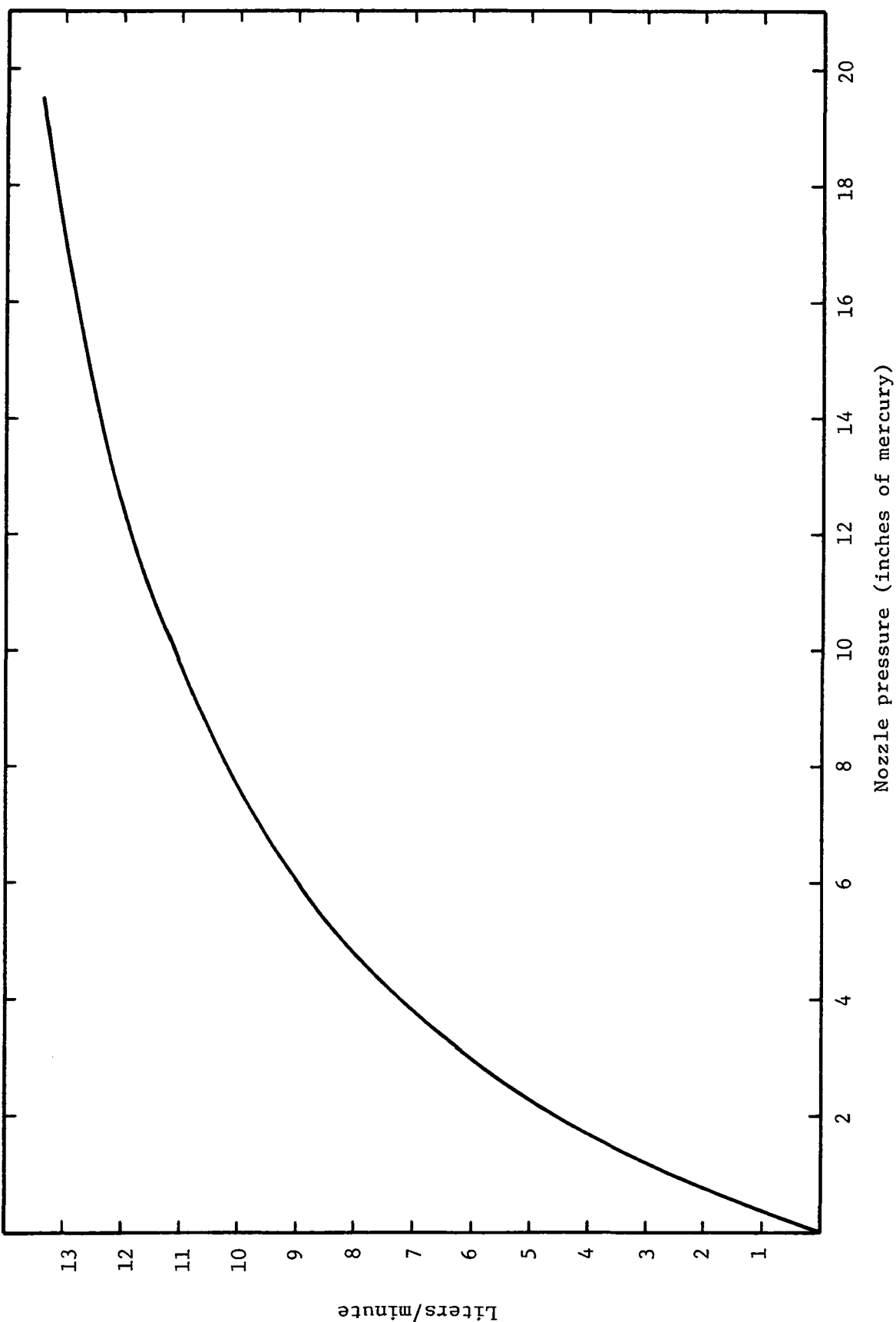


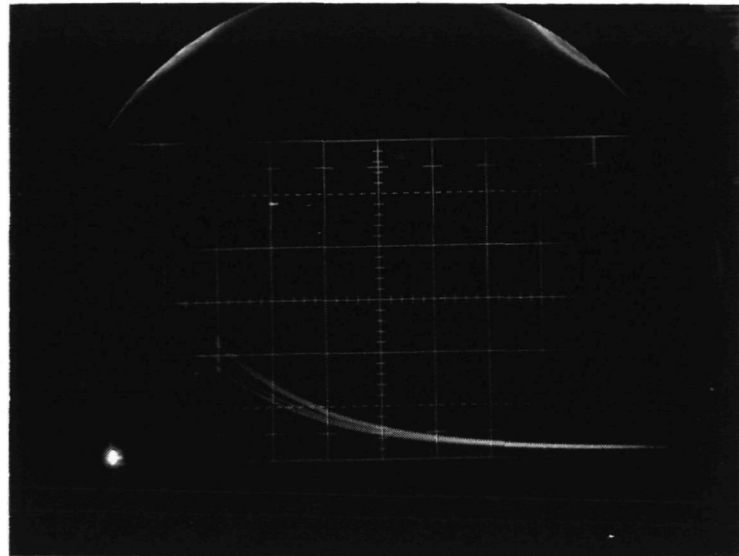
Figure 11. Sampling Characteristics of Vacuum Nozzle Particle Accelerator

7.0 MOS ELECTRONICS

The MOS particle sensor is, in effect, a MOS capacitor having the silicon substrate as one plate, the SiO_2 film as the dielectric, and a 500 \AA film of evaporated aluminum as the other plate. A DC bias, supplied by a battery, is placed across the MOS capacitor through a 1000Ω resistor. When a particle strikes the MOS sensor with sufficient momentum to cause damage of sufficient magnitude in the dielectric, the capacitor discharges through the dielectric. The capacitors are connected in parallel to obtain large counting areas with the added benefit that the parallel connection provides added charge, hence current density, to burn away the aluminum in the damaged area. The time for this clearing operation is on the order of nanoseconds as shown by the rise time in Figure 12. The battery then recharges the capacitor through the 1000Ω resistor and thus reestablishes the electric field across the capacitor as shown by the fall time of the pulse in Figure 12. A portion of the recharge current is fed to a Fairchild $\mu\text{A}-710$ comparator circuit. Since there is a variation in the amplitude of the recharge pulses, which depends upon the applied bias and to some extent upon the impact event, this circuit is necessary in order to supply constant amplitude pulses to the HP 25456 electron counter. For most instances, the amplitude of the discharge pulse is approximately 25 percent of the applied bias. A schematic diagram of the MOS readout circuit is shown in Figure 13. Shown below is a sample calculation of the capacitance and maximum counting rate of the MOS sensors.

$$C(\text{pf}) = 8.85 \times 10^{-2} \frac{(K)(A)}{d} \quad (1)$$

1 v/div



0.2 μ s/div

Figure 12. MOS Discharge Pulse.

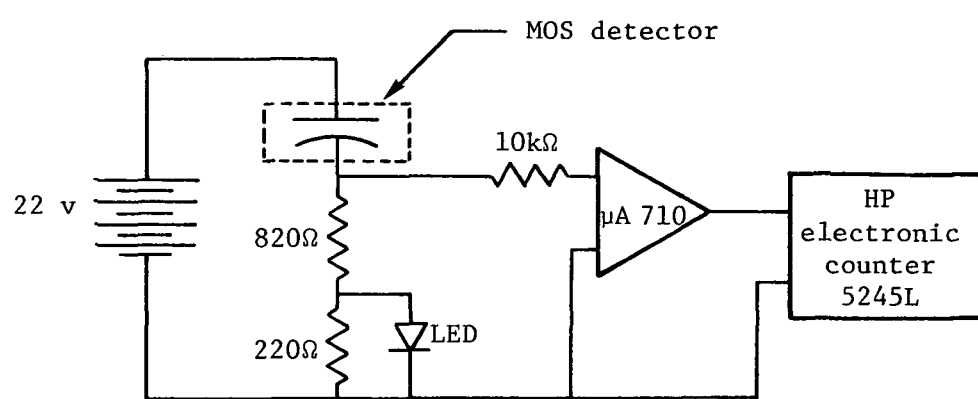


Figure 13. Schematic Diagram of the MOS Readout Circuit.

where $K = 3.2$ for SiO_2

d = dielectric thickness in centimeters

A = area in cm^2 .

For a 15-mil diameter MOS unit, the area is $1.14 \times 10^{-3} \text{ cm}^2$. With a thickness of 1000 \AA (10^{-5} cm), the 15-mil diameter MOS capacitor has a capacitance of 32.3 picofarads. Assuming that eleven units are connected in parallel, as in most instances, the total capacitance, C_T , is 355 picofarads. Thus the RC time constant for recharging the impacted sensor is

$$RC = (1 \times 10^3 \Omega)(355.1 \times 10^{-12} \text{ f}) = 0.355 \times 10^{-6} \text{ sec.}$$

Allowing one RC time constant for each counting event yields

$$f = \frac{1}{P} = \frac{1}{0.355 \times 10^{-6} \text{ sec}} = 2.8 \times 10^6 \text{ maximum counts/sec.}$$

Below is a table showing the effect of SiO_2 thickness on the MOS capacitance and maximum counting rate.

SiO_2 thickness	C	C_T	RC	f
700 \AA	46.1 pf	507.1 pf	0.51 μsec	1.96×10^6
1000 \AA	32.3 pf	355.3 pf	0.36 μsec	2.77×10^6
1200 \AA	26.9 pf	295.9 pf	0.29 μsec	3.39×10^6

8.0 DATA-GATHERING METHODS

The calibration procedure was carried out by simultaneously sampling from the particle generation system with the vacuum nozzle particle accelerator and the Climet Model CI-250 particle counter acting as a reference. The calibration setup is illustrated in Figure 14.

At the beginning of each set of runs, the background of the system was checked by using isopropyl alcohol in the particle dispensing system and sampling simultaneously with the Climet particle counter and the MOS sensor in the vacuum nozzle particle accelerator. In general, the Climet would indicate a background count which the MOS would not. The background for the Climet could then be subtracted from the Climet counts obtained from the runs made with a particle-saturated solution to obtain the correct number of counts to be used as a standard for comparison with the MOS counts. Each time a run with different size particles was made, the dispensing system was completely cleaned and the background was checked.

The three basic types of data taken were (1) threshold data, (2) variable pressure data, and (3) variable bias data. In addition, a preliminary evaluation as an environmental monitoring instrument was conducted by mounting a MOS unit aboard an aircraft and flying through the emissions from power plant smoke stacks in Virginia and North Carolina. The variables examined during these series of tests were dielectric (SiO_2) thickness, particle size, particle velocity, sampling rate, and MOS bias voltage. The three dielectric thicknesses investigated were 700 \AA , 1000 \AA , and 1200 \AA ; and the diamond particle sizes investigated were 1 μ , 3 μ , 6 μ , and 9 μ .

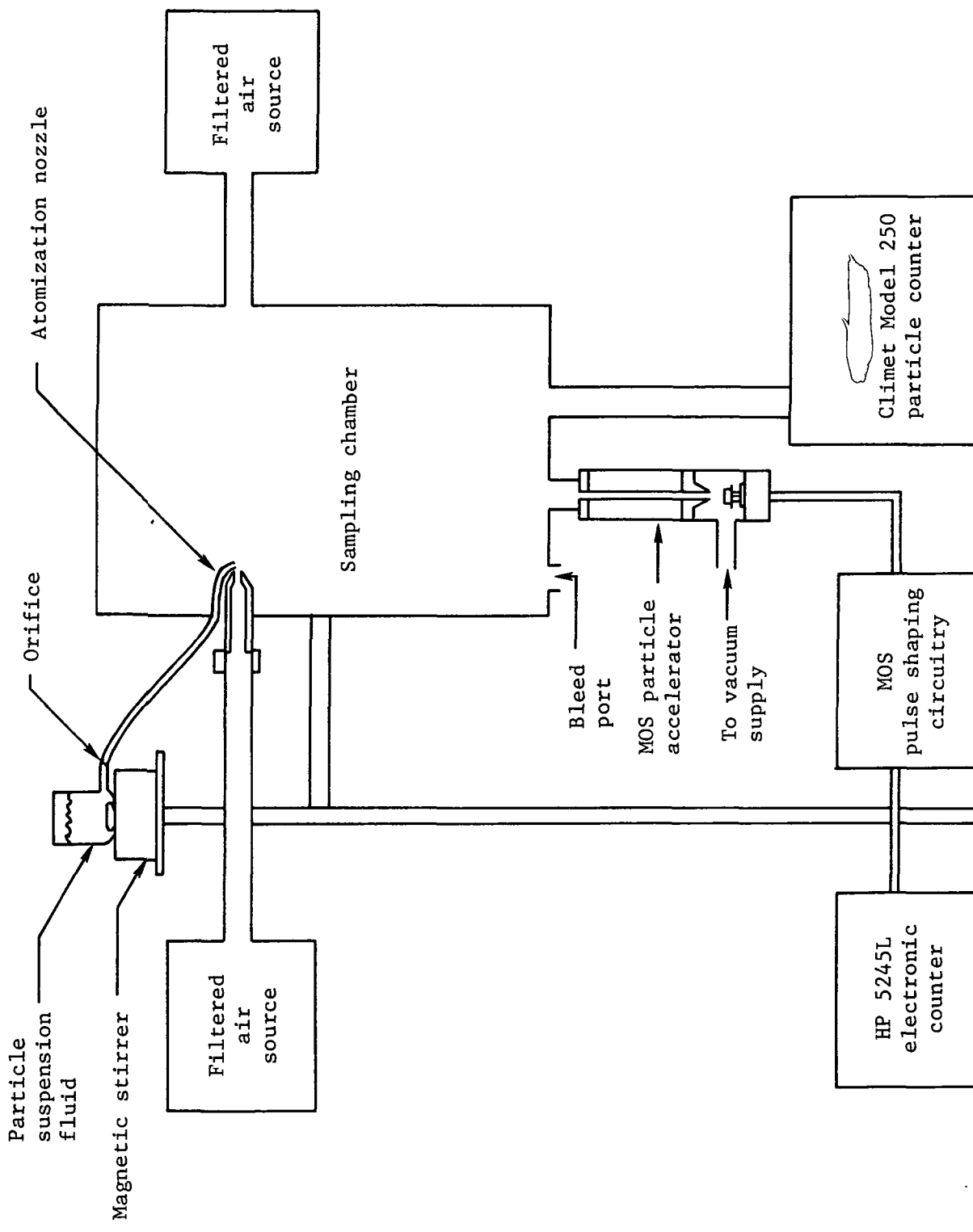


Figure 14. A Schematic Representation of the Calibration System.

8.1 THRESHOLD DATA

The threshold data were obtained to determine a mass-velocity relationship for particle counting by a MOS sensor with a given dielectric thickness. Threshold data were obtained for the 700, 1000, and 1200 \AA silicon oxide thicknesses and for 3-, 6-, and 9-micron diamond particles. With the MOS sensor biased at a given voltage, the threshold for counting was determined by starting with the MOS vacuum nozzle particle accelerator velocity at zero and then slowly increasing the nozzle pressure, thus the particle velocity, until the MOS sensor began to count. For each set of conditions--bias, particle size, and SiO_2 thickness--the counting threshold nozzle pressure was obtained ten times and then averaged. The nozzle pressure was converted to a particle velocity using the theory in Appendix A. The graphical representation of the theory used is displayed in Figure 15 where the ratio of nozzle pressure to atmospheric pressure is along the horizontal axis and the particle velocity is along the vertical axis. The V_{p3} 's are the exit velocities. The family of curves represents different particle diameters of density 3.5 gms/cm³ (diamond). The particle diameter-mass relationship for diamond is shown in Figure 16. The threshold data for MOS sensors with 700, 1000, and 1200 \AA SiO_2 dielectric are shown in Figure 17. In each case the electric field in the dielectric was 2.2×10^6 volts/cm. The diameter of the particle associated with the threshold was assumed to be 3, 6, or 9 microns depending upon the particle distribution chosen for the particular experiment. By collecting a sample upon a slide inserted in the bottom of the sampling chamber and observing the slide under a microscope, the large particles observed in each case were near 3, 6, or 9 microns.

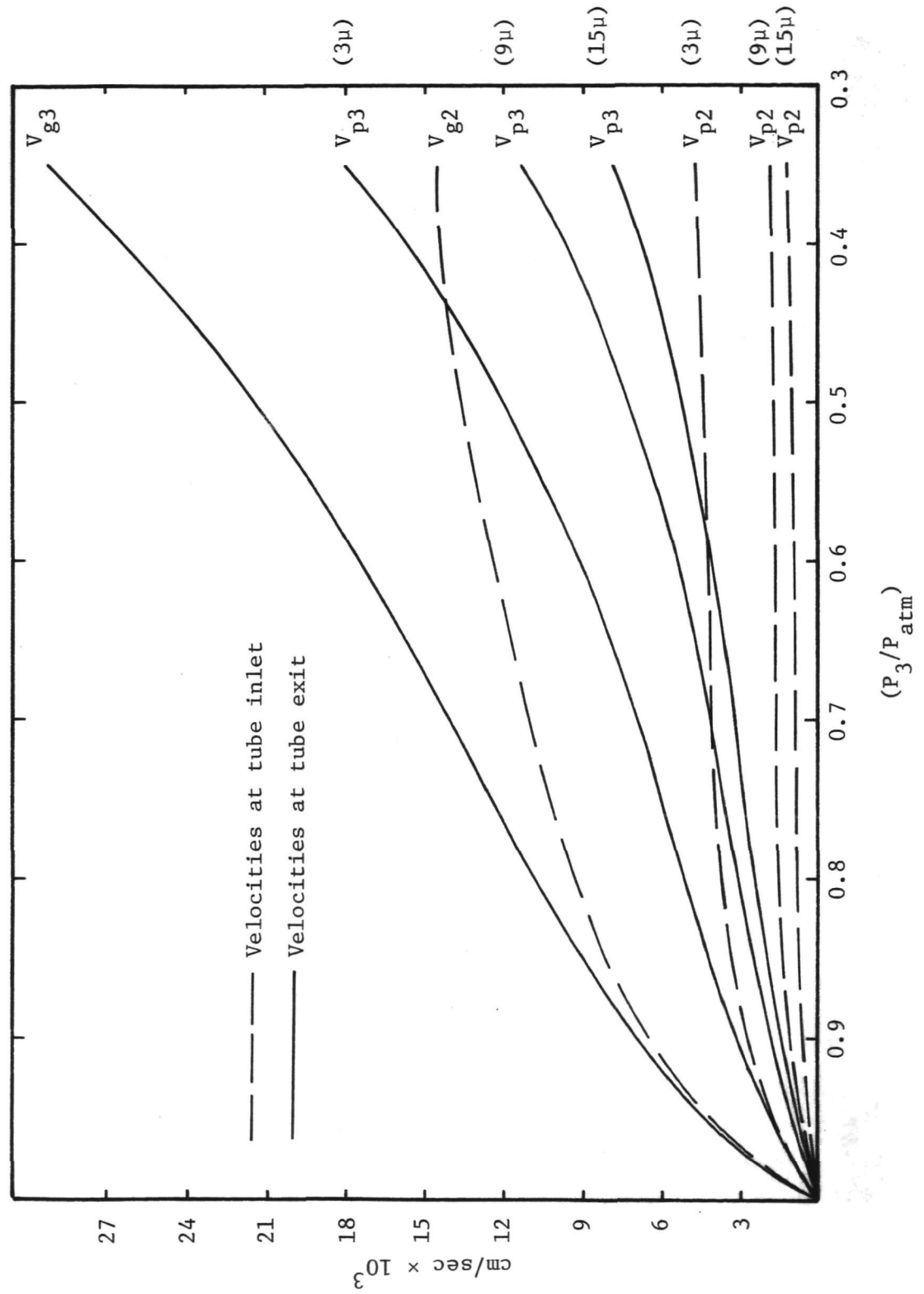


Figure 15. Particle Velocity as a Function of Particle Accelerator Nozzle Pressure (3μ , 9μ , and 15μ Diameter Particles).

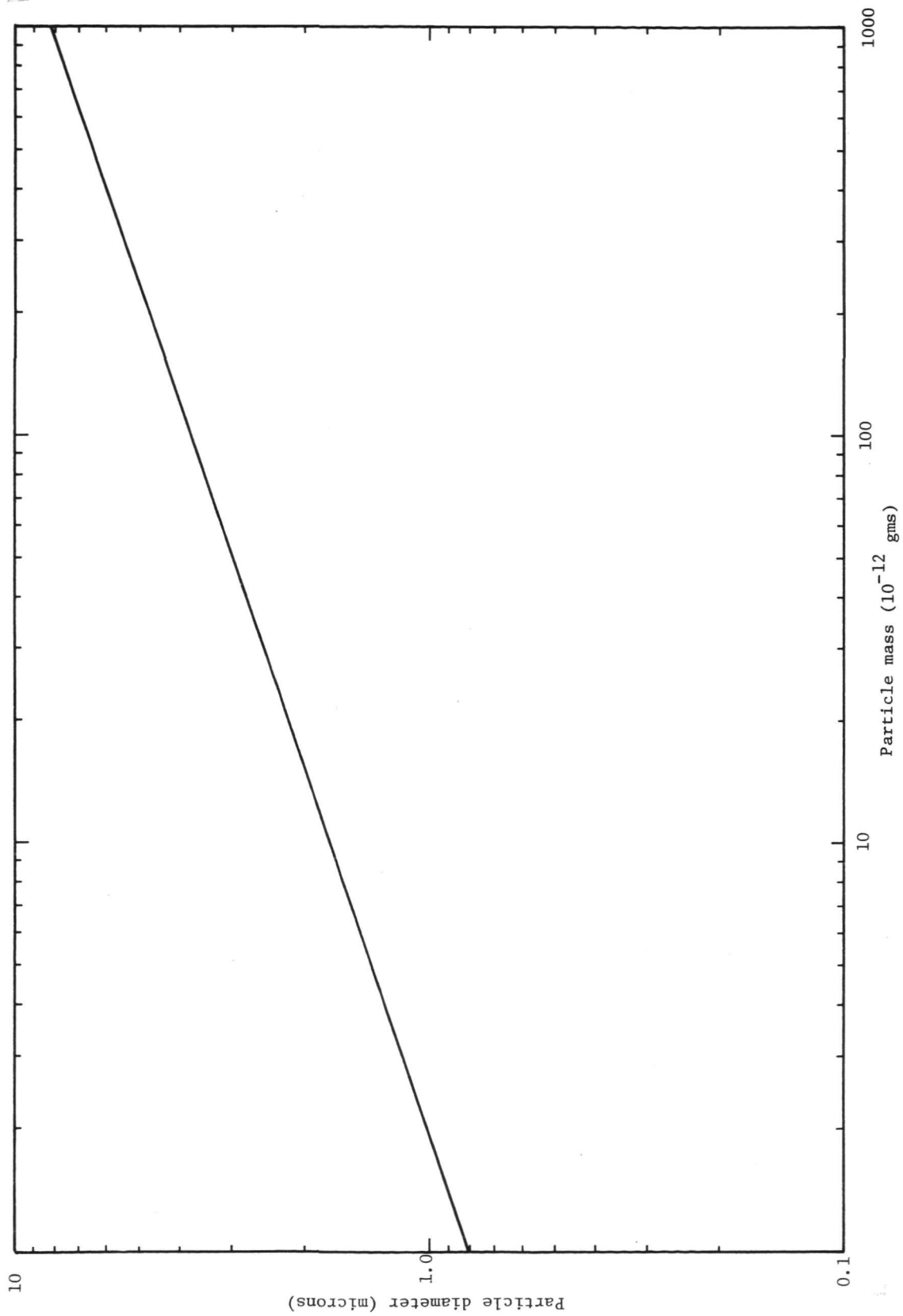


Figure 16. Particle Diameter-Mass for Diamond Microparticles.

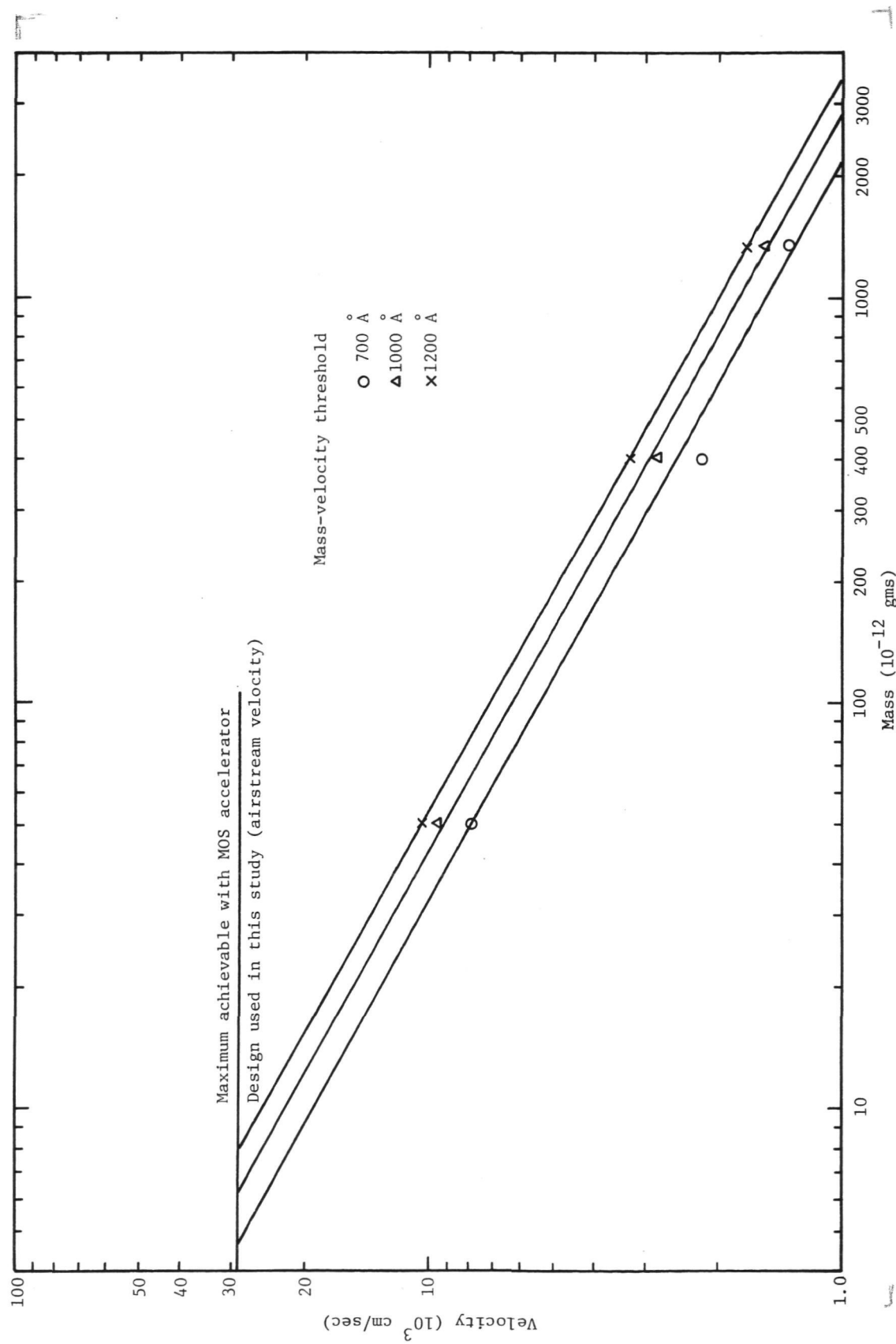


Figure 17. Particle Mass-Velocity Threshold for Initiating MOS Capacitor Discharge.

8.2 VARIABLE BIAS DATA

Variable bias data were taken to determine the effect of an electric field upon the threshold of counting for the MOS sensor. Observing the threshold for several bias voltages with each particle distribution and with each thickness of SiO_2 resulted in the data included in Figure 18. The straight lines represent a theoretical interpretation of the data to be discussed in a later section.

8.3 VARIABLE PRESSURE DATA

The variable nozzle pressure data were taken to determine the counting efficiency of the MOS sensor relative to the Climet instrument. In addition, the particle size selectivity of the MOS can be inferred assuming a correlation between the instruments exists and assuming a consistent model for the operation of the MOS can be discerned. A typical set of data is shown in Figure 19. These data were obtained by varying the nozzle pressure and noting the MOS particle count. At least five separate observations at each nozzle pressure were averaged to obtain each data point shown in Figure 19. Each observation was for a 36-second sampling interval. For each sampling interval a Climet reading in either the 5- or 2-micron range was obtained. For the particular range the instrument counts all particles about that setting. Since the volume of air sampled by the Climet and the MOS in the 36-second interval differed, a correction factor to obtain a meaningful comparison was introduced. Basically, the average of the Climet counts was multiplied by the ratio of the volume of air sampled by the MOS to the volume of air sampled by the Climet. In addition, the MOS counts were corrected for the fact that the active area of the device is only a fraction of the area intercepted by the sampled air stream. An example of the area effect can be seen in Figure 20, where

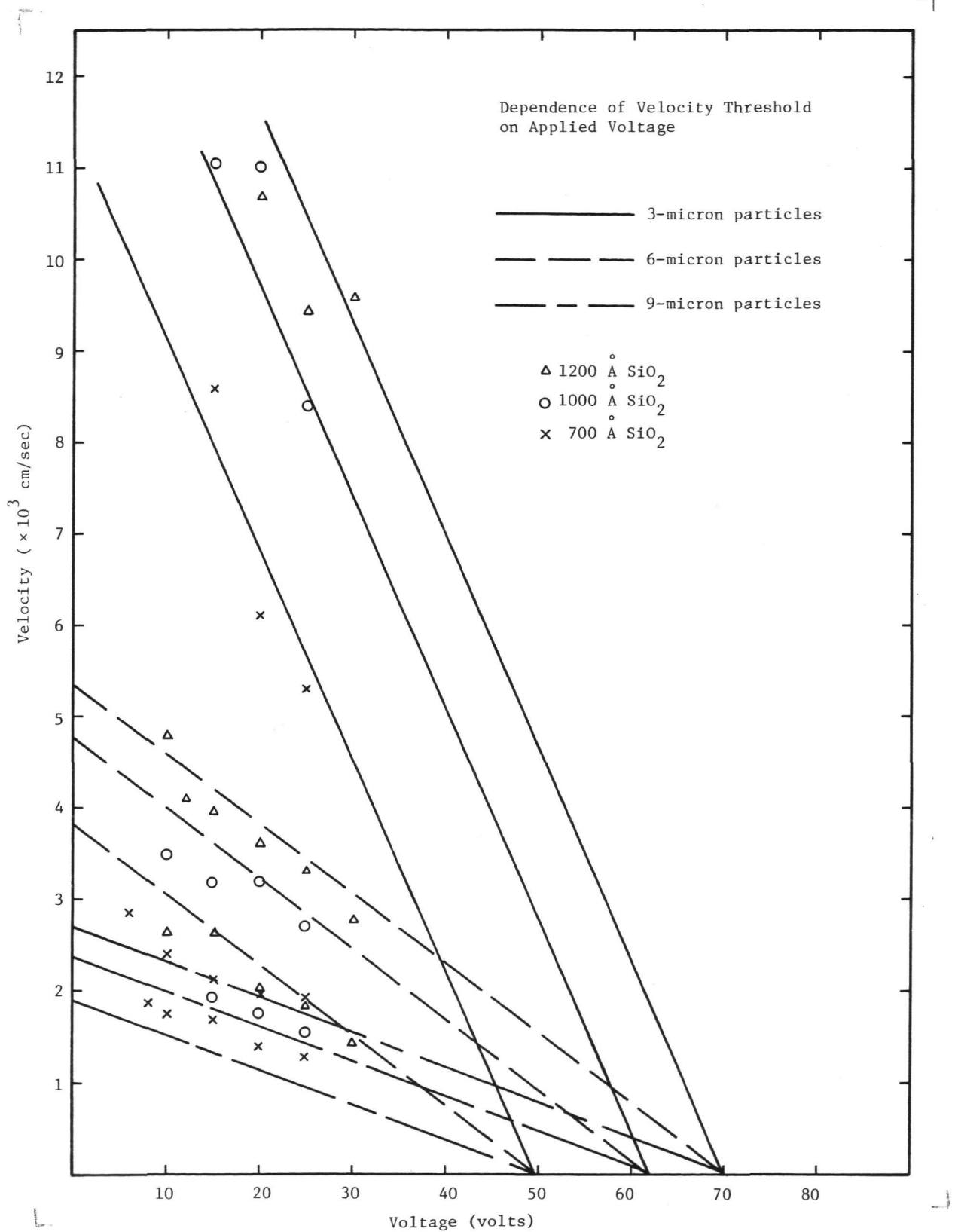


Figure 18. Dependence of Velocity Threshold on Applied Voltage.

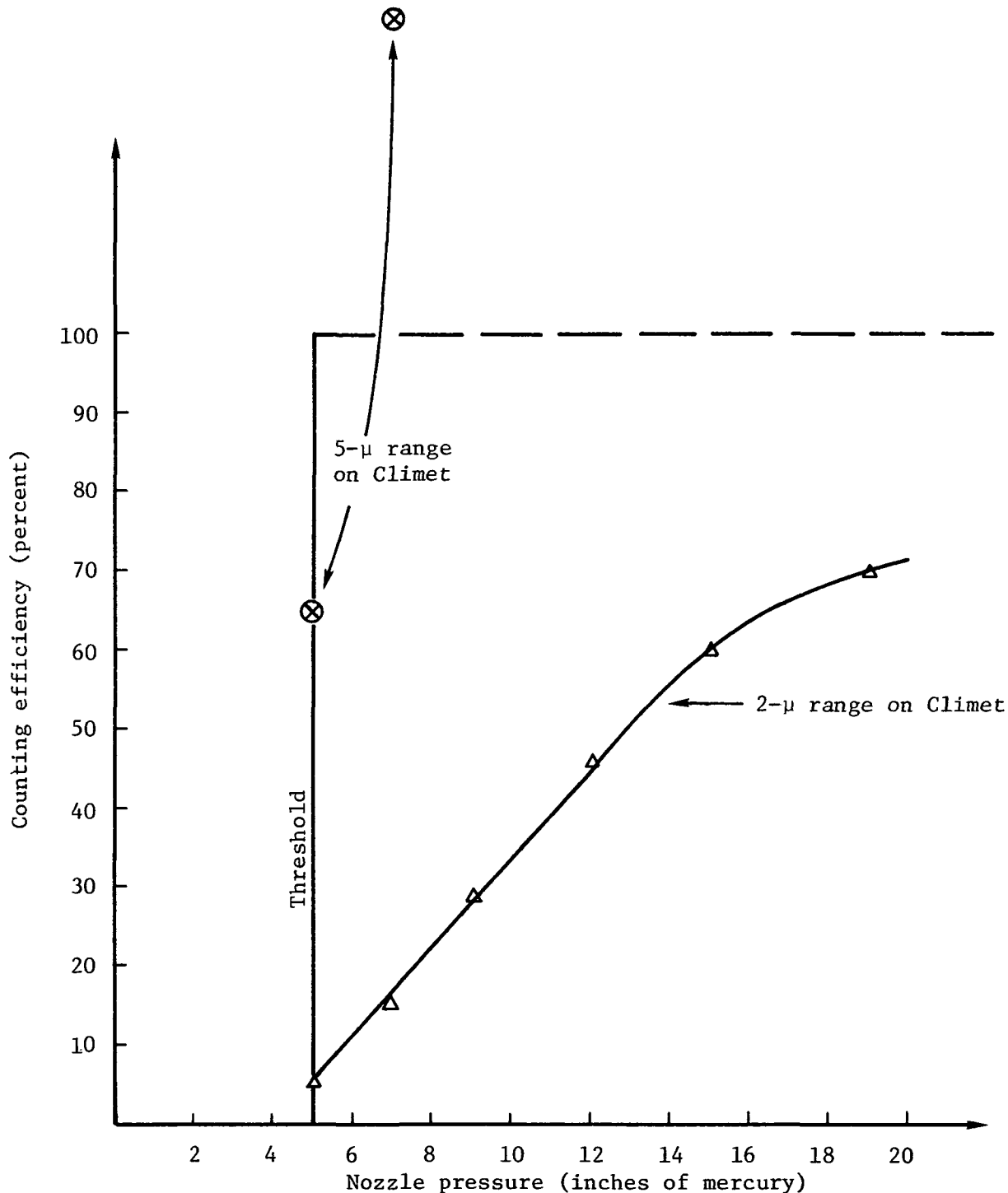


Figure 19. MOS Counting Efficiency Relative to Climet 6-micron Particle Distribution (1200 \AA SiO_2)

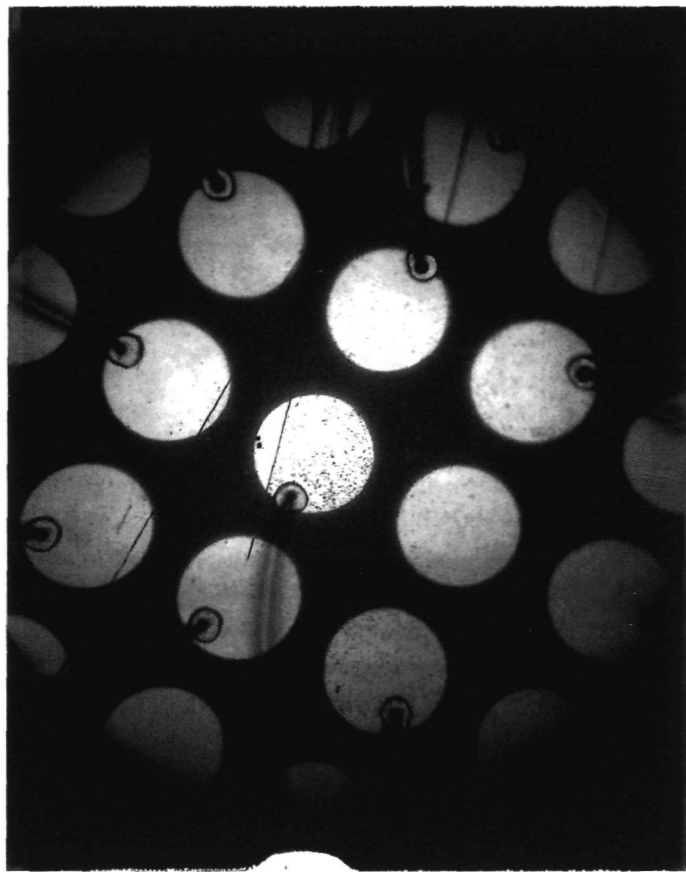


Figure 20. Photomicrograph of Impacted MOS Sensor.

the number of 15-mil dots that show a preponderance of counts is limited to three or four units. Using simple geometric considerations as shown in Figure 21, the average of the MOS counts at each nozzle pressure was corrected. Through actual examinations of the surface of an impacted MOS sensor, it was determined that somewhere between three and seven of the 15-mil MOS units did most of the counting. Thus the MOS counts should be multiplied by a factor between approximately 2 to 4. Numerous observations led to the use of the larger correction of 4. Using the above procedures certainly limits the accuracy of the results; however, qualitative interpretation predicated on these results will be given in a later section.

8.4 IN-FLIGHT SENSOR EVALUATION

The purpose for conducting the in-flight tests of the MOS sensors was to determine the ability of these sensors to function as useful instruments for environmental monitoring.

A Cessna 182 was chartered for use on these test flights. Two vacuum nozzle particle accelerators were mounted on the wing spar. The particle intake ports were aimed toward the rear of the plane to prevent dust from the runway from damaging the MOS sensor during takeoff. A triggering circuit, illustrated in Figure 22, was designed and used with the normal MOS sensor circuitry in order to trigger a strip chart recorder which acted as an event counter. The AC power for the vacuum pump and the electronic equipment was supplied by two 12-volt wet cell batteries and a 500-watt inverter. The MOS sensors used for these tests were the 4×4 array, 15-mil diameter dot type with 500 \AA aluminum contacts. The SiO_2 dielectric thicknesses were 700 and 1200 \AA . A block diagram of the equipment used for these tests is shown in Figure 23.

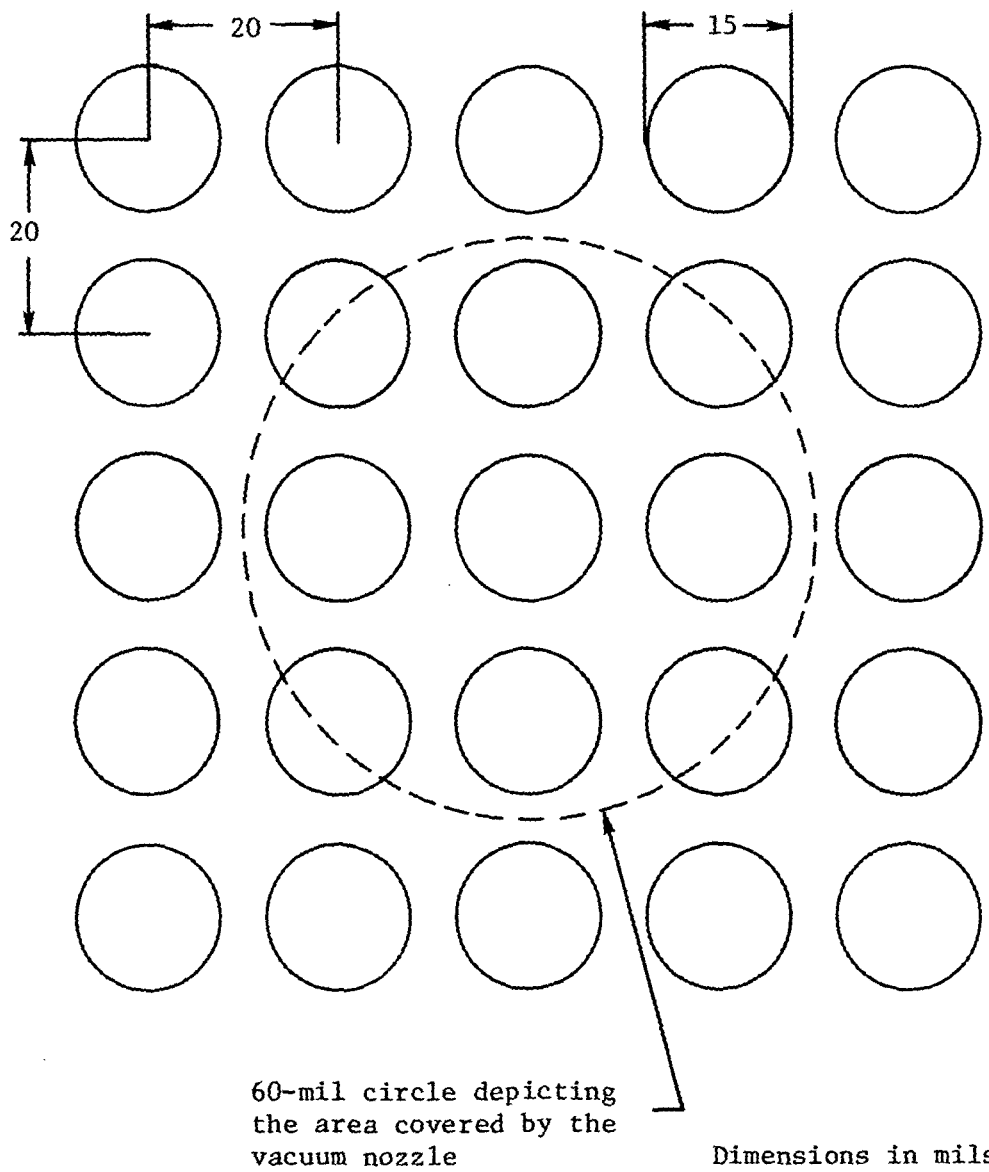


Figure 21. Illustration of Geometrical Considerations
to Determine Counting Efficiency.

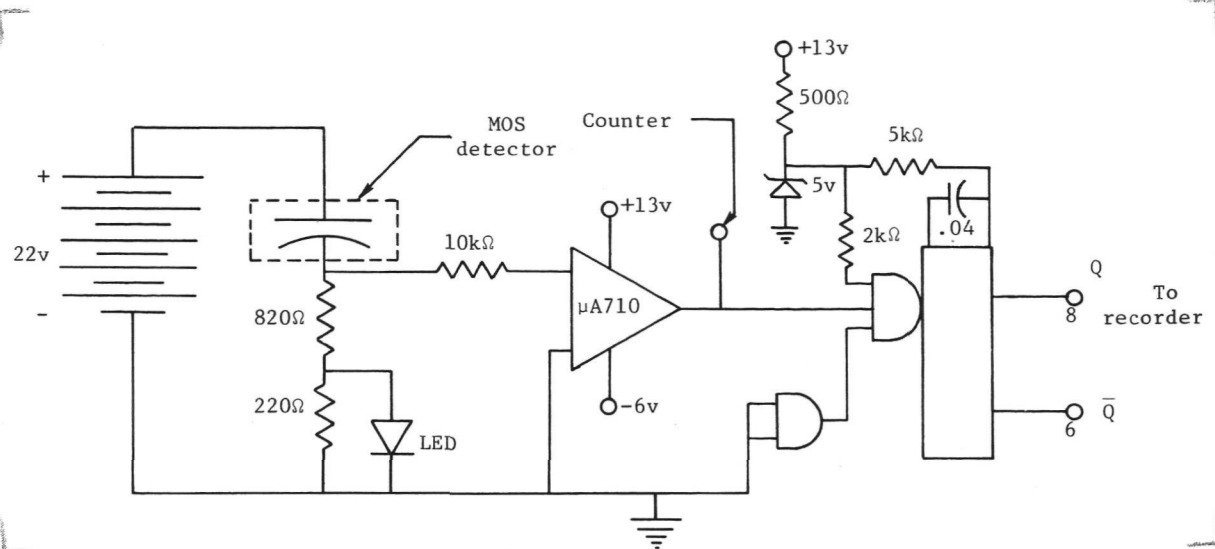


Figure 22. Schematic of MOS Sensor Counting Circuit Used in Flight Evaluation.

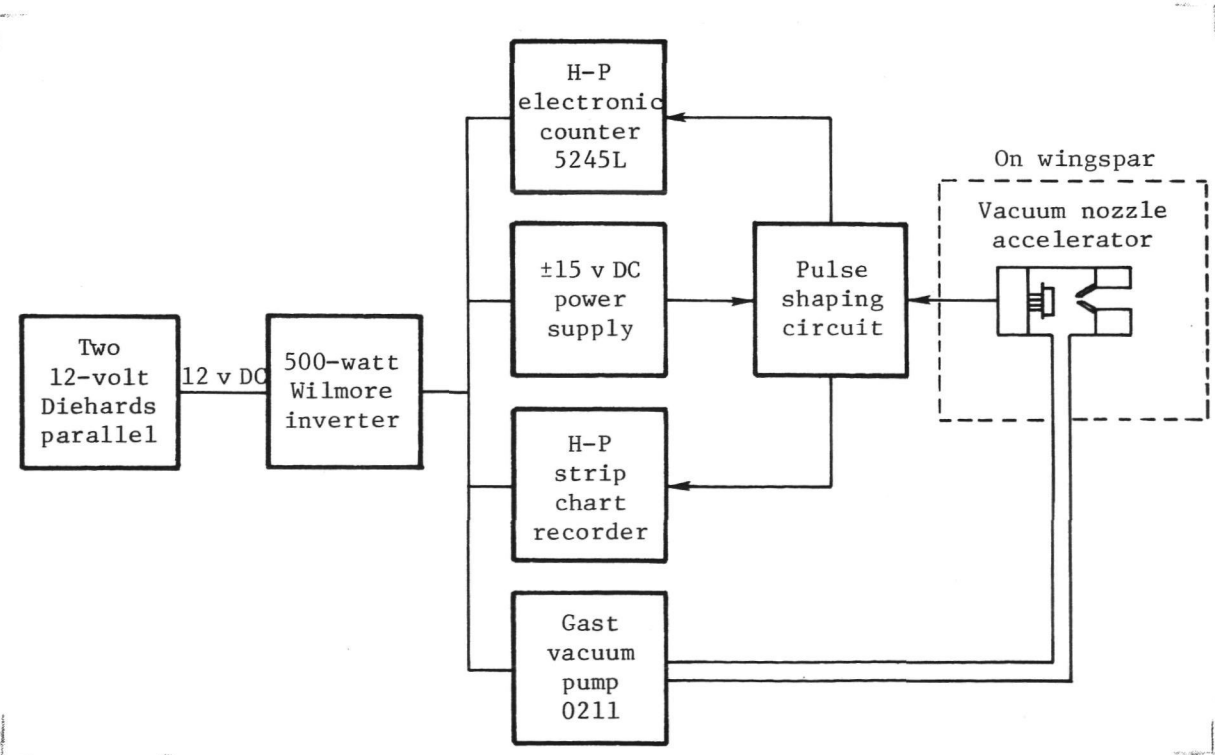


Figure 23. Block Diagram of MOS Sensor Counting System.

Since the MOS particle sensors had individual lead-in cables and vacuum lines, either the 700 Å or the 1200 Å sensor could be easily switched into the counting circuitry.

The MOS particle sensors were in operation during the flight from the Raleigh-Durham Airport to Langley Field and on the return trip to Raleigh-Durham. Three flights were made from the Langley Field over the Yorktown area. The flights were made at altitudes ranging from 500 to 1100 feet. The particle counting rate was largest at 500 feet and dropped off with increasing altitude. Particle counts were recorded more than 2 miles downwind from a coal-fired power plant. The visible plume from the source was approximately 1000 feet high; however, the larger counting rate at 500 feet indicated that the larger particles had settled out of the plume. Fourteen counts were recorded with a 1200 Å MOS sensor as the stack was approached from downwind at 1000 feet altitude, with the highest rate of counting being approximately 0.5 mile from the stack. At an altitude of 800 feet, an identical approach was made toward the stack, and a total of 61 counts were recorded. When the 1200 Å MOS sensor was flown at 500 feet at right angles to the plume, 523 counts were recorded. The counting rate at 500 feet with a 700 Å MOS sensor was of sufficient magnitude to destroy the sensor after a few seconds of counting.

A light rain occurred between the second and third flights, and the particle counting rate dropped off by approximately a factor of ten. The rain droplets apparently condensed on the particles and thus cleaned the air as the rain fell. No evidence of corrosion of the metal (aluminum) contacts was observed, indicating that this anticipated problem did not materialize.

A flight over a North Carolina coal-fired electric power plant yielded data with both the 700 Å and 1200 Å MOS sensors that were very similar in magnitude and altitude conditions to those recorded in Virginia. A photograph showing the mounting arrangement on the wing spar of the aircraft is shown in Figure 24.

NASA
L-74-539



Figure 24. Photograph of MOS Sensor on Wing Spar of Aircraft.

9.0 ANALYSIS

To facilitate calibration of other MOS units, a consistent model which relates the experimental observations in the present effort will be presented. The threshold data in Figure 17 suggest a rather classical penetration relationship where

$$x_p = k m^\lambda v^n \quad (2)$$

where x_p is the thickness penetrated by a particle of mass m and velocity v . A reasonable assumption to explore is that penetration through the aluminum electrode and the dielectric is required to initiate an electrical discharge. However, two observations are not included in such a simple model. First, it has been observed that the threshold is dependent upon the applied bias. As voltage is increased, the threshold velocity for a given particle mass decreases. For typical data in Figure 17 the particle energy is near 10^{-10} joules while the energy stored on the capacitor is near 10^{-7} joules. Thus the electrical energy is between 100 and 1000 times the kinetic energy of the particle. Thus the added particle energy as the velocity is increased does not replace the reduction in electrical energy with reduced applied voltage. Secondly, a rather unique feature of the operation of the MOS units is that for applied voltages less than 7 volts, a particle impact results in a short which will not clear. This lower limit of operation is independent of oxide thickness at least for the units used in this study.

Another factor which will be useful in characterizing the operation of the MOS sensor is the inherent electrical field strength for the silicon

oxide. In numerous observations the units would spontaneously discharge when the electrical field was between 3 and 4×10^6 volts/cm. Detailed studies of electrical breakdown in SiO_2 report values from 10^6 to 10^7 volts/cm. At the lower values it is generally recognized that small defects in oxide are responsible for the discharges. The electrical discharges are indistinguishable from the microparticle-initiated discharges and clearly must be avoided. Thus the range of operation is bounded on the lower end by the non-clearing events at about 10^6 volts/cm and on the upper end by the spontaneous electrical discharges at about 3×10^6 volts/cm.

Although the present understanding evolved in a rather circuitous manner, the penetration-type relationship involving mass-velocity suggested that a well defined penetration was required. The voltage dependence of threshold suggested that penetration to a depth where the electrical field in the unpenetrated oxide exceeded the field strength for breakdown should be considered. A simple illustration of the geometry of the penetration is shown in Figure 25. As the particle penetrates to depth X_p , it is assumed that aluminum is carried along to provide electrical continuity such that the applied voltage appears across X_3 . When the depth of penetration is such that the field in X_3 exceeds the field strength of the oxide, a discharge will occur. A rather tenuous assumption of a field strength near 10^7 volts/cm could be used to proceed. However, the data in Figure 18 can be used to infer a value for the field strength. Assuming a penetration relationship for threshold of particle-initiated discharges where

$$X_p = k m^\lambda v^n \quad (3)$$

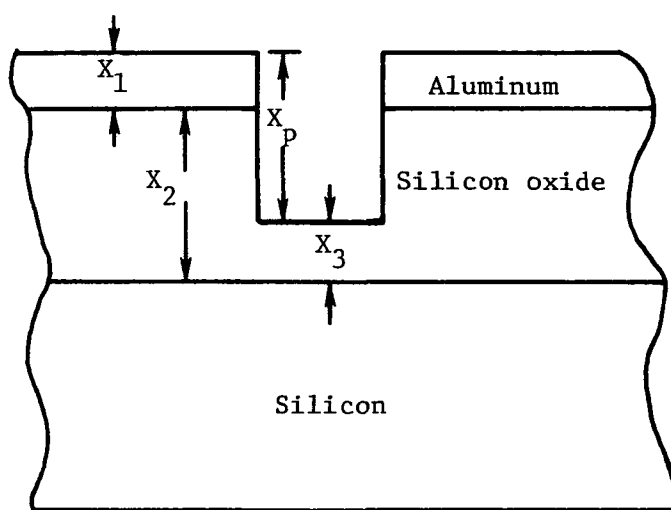


Figure 25. Illustration of the Particle Penetration Geometry.

and a field strength for discharge events (E_d) where

$$E_d = \frac{V}{X_3}, \quad (4)$$

the dependence of threshold velocity upon applied voltage is given by

$$V = -E_d k m^\lambda v^n + E_d (X_1 + X_2). \quad (5)$$

Without attempting a detailed fit to the data, a value of $E_d = 4 \times 10^6$ volts/cm was used. Partial justification for the choice was the observations of spontaneous discharge near 4×10^6 volts/cm. While field strengths near 10^7 volts/cm have been reported, the impact event may damage the unpenetrated region resulting in a lower field strength. In any event, the value of 4×10^6 volts/cm provides a reasonable lower limit. After assuming a value for E_d , it is straightforward to find X_p for the mass-velocity relationship in Figure 17. Since the data were taken at equal applied electric fields of 2.2×10^6 volts/cm, the ratio X_2/X_3 is given by

$$\frac{X_2}{X_3} = \frac{4 \times 10^6}{2.2 \times 10^6} = 1.8. \quad (6)$$

Therefore,

$$\begin{aligned} X_p &= X_1 + X_2 - X_3 \\ &= X_1 + X_2 - \frac{X_2}{1.8} = X_1 + 0.44 X_2. \end{aligned} \quad (7)$$

The thickness of the aluminum electrode was 500 Å in every case. The penetration threshold with an applied electric field of 2.2×10^6 volts/cm for the three SiO_2 thicknesses is given in Table 2.

Table 2. Particle Penetration Threshold for Various Silicon Oxide Thicknesses with Electric Field of 2.2×10^6 volts/cm

SiO_2 thickness x_2	Penetration thickness x_p
700 Å	810
1000 Å	940
1200 Å	1030

Using the penetration thicknesses in Table 2 to obtain a fit to the data in Figure 17 results in

$$x_p = 8.5 \times 10^{-4} m^{0.54} v \quad (8)$$

where x_p is in centimeters, m is in grams, and v is in centimeters/second. This linear dependence of penetration on velocity has been previously observed for impacts at low velocities.^[1]

Using the results in Equation 8 and a value of $E_d = 4 \times 10^6$ volts/cm, a set of theoretical curves have been drawn in Figure 18. Some adjustment in E_d may result in a better fit; however, the adjustment would appear to be less than 10 percent based on the data for 6-micron particles. However, the 9-micron particle data are a bit high and suggest a slight increase. It should be pointed out that the data were taken on a number of units, and any variations in the field strength from unit to unit will influence

the results. Therefore, some of the scatter in the data may result from variations in electrical properties. As mentioned earlier, the particle distributions are not sufficiently characterized to provide precise analysis; therefore, the theoretical curves are considered reasonable under the circumstances.

10.0 DISCUSSION

The calibration data in Section 8 and the analysis in Section 9 can be combined to provide an interpretation of the counting efficiency of the MOS relative to the Climet and to provide an estimate of the minimum particle diameter counted by the MOS. With a given bias on the MOS, the impacting particle must penetrate well into the oxide to initiate breakdown. For the MOS particle accelerator analyzed in Appendix A, the velocity of the impacting particles is dependent upon the particle diameter. Thus at a given nozzle pressure, only particles of a certain diameter or greater will achieve the penetration threshold for discharging the MOS capacitor. The accelerator is essentially a mass selector in terms of threshold since an increase by a factor of ten in mass results in less than a factor of three change in velocity for a given nozzle pressure in Figure 15. If all particles impacted with identical velocities, the mass selectivity would be very precise. However, the threshold of penetration is approximately equal to the square root of the particle kinetic energy; thus a range of particles will have the same threshold of penetration for the MOS unit. Since the particle mass varies as the cube of the diameter, the threshold of penetration in terms of particle diameter will have a much narrower range. For a given nozzle pressure in the range of interest, $0.7 < (P_3/P_{atm}) < 0.95$, the particle velocity decreases approximately as the inverse square root of the particle diameter, or

$$v_p \sim \frac{1}{d^{1/2}}.$$

Thus the threshold penetration varies essentially as

$$x_p \sim (m v_p^2)^{1/2} \sim d \quad (18)$$

or directly proportional to particle diameter. This simply means that as the nozzle pressure is increased, the threshold will be determined by the largest diameter particles present in the sampled air volume. This assumes that the pressure is increased slowly enough that the relative occurrence of the particle diameters does not influence the measurement. Another way of stating this assumption is that over the observation time, all particles of various diameters in the sampled volume of air should impact a MOS capacitor.

The counting efficiency observed for the 6-micron particle distribution shown in Figure 19 can be explained in terms of the threshold of penetration dependence on particle diameter. As the nozzle pressure is increased, a threshold at 5 inches of mercury is due to the largest diameter particle in the particles sampled. By direct observation of particles collected on a glass slide, this particle diameter is near 6 microns. The Climet reading for particle diameters greater than 5 microns is used as a standard, and the MOS counts 65 percent of the greater than 5 micron particles at the threshold. As the nozzle pressure is increased, the MOS counts not only particles greater than 5 microns but also particles less than 5 microns in diameter, hence an efficiency greater than 100 percent since the 5-micron range on the Climet is used as the standard. Changing to the greater than 2 micron range on the Climet, an increase in nozzle pressure continues to increase the counting efficiency. This increase is due to the fact that the particles are distributed in diameter and as the

nozzle pressure is increased, smaller diameter particles reach the threshold of penetration and initiate a capacitor discharge. The fact that the MOS counted only 70 percent of the Climet counts may be due to either one of two possibilities: The precision of the data must surely be in question considering the uncertainties in the conversion factors used to provide a meaningful comparison between the Climet with the MOS, or there could be 30 percent of the particles greater than 2 microns which do not achieve the threshold of penetration. Assuming the model is consistent, the smaller particles near 2 microns would constitute the 30 percent not counted. Using the data in Figure 15 and interpolating the velocity for a 2-micron particle at 19 inches of mercury indicates that the threshold of penetration is achieved; thus the 30-percent difference may simply be due to the lack of precision in correcting the data.

The lower limit for counting with the MOS unit designed and employed for these calibration studies can be inferred. The airstream velocity is approximately 2900 cm/sec at 19 inches of mercury which is the maximum achievable velocity for the present design. Assuming the particles could be accelerated to this maximum velocity, the 700 \AA SiO_2 unit would count all particles greater than 1.4 microns in diameter, the 1000 \AA SiO_2 would count all particles greater than 1.5 microns in diameter, and the 1200 \AA SiO_2 would count all particles greater than 1.6 microns in diameter. Since the particles do not achieve airstream velocity, the lower limit is somewhat larger than the above values; however, smaller than 2 microns. To provide a test of these conclusions, a distribution of small particles which contains no particles greater than 2 microns was impacted against the 1000 \AA MOS units. The nozzle pressure was increased to 19 inches of mercury; however, the MOS unit did not count. Climet readings were used to determine

the particle size distribution. To insure that the MOS counter would count, a distribution containing greater than 2 micron diameter was impacted. The MOS unit did respond to the distribution containing greater than 2-micron diameter particles.

Regarding the observation that polystyrene particles do not discharge the MOS sensor, classical penetration theory would include the effect of the density of the particle and the density of the target material. In fact, two particles of density ρ_1 and ρ_2 impacting identical targets at identical velocities would result in ratios of penetration given by^[1]

$$\frac{X_{p1}}{X_{p2}} = \sqrt{\frac{\rho_1}{\rho_2}} .$$

Thus less dense particles penetrate less than the denser particles. Part of our observations may be simply explained by the density of the particles. However, in some instances with large organic crystals (~ 10 microns) which did not initiate discharges, the density of the particle does not account for the failure to initiate a discharge. These observations suggest that hardness must also be considered. We propose that brittle particles absorb some of the energy of the impact by shattering at impact, thereby reducing the energy available for the penetration. However, to validate the observation and the explanation will require further study.

Finally, the shorting of the capacitors observed in this study when the applied bias is reduced to approximately 7 volts and threshold of velocity should be considered. For the different particles, they must achieve the penetration threshold X_p regardless of particle size. At 7 volts the threshold penetration is approaching complete penetration;

hence the discharge is not initiated by dielectric breakdown but by leakage through a damaged dielectric. It is possible that the lack of a sharp rise time for the discharge precludes the rapid rise in local temperature, hence the lack of vaporizing the aluminum carried through by the particle. In any event, the unpenetrated dielectric which is assumed to be damaged and leaky rather than insulating increases by 30 percent from a 700 \AA SiO_2 film to a 1200 \AA SiO_2 film. Considering the lack of precise control of particle velocity and size which impacts the unit with near threshold penetration, it is unlikely that a 30-percent variation when shorting is the ultimate observation can be established. In conclusion, it is unlikely that data can be obtained with sufficient precision to see the 30-percent variation. However, the range from 7 to 8 volts as the applied bias which will result in shorted MOS units has been repeatedly observed.

REFERENCE

- [1] Goldsmith, Werner, "Analytical Versions of Penetration Processes." Dept. of the Navy, Naval Ordnance Test Station. NAVWEPS Report 7812, NOTS Technical Publication 2811 (February 1962).

11.0 APPLICATION

In this report we have reported on the design, testing, and calibration of a MOS particulate detector. Numerous variations in detector housing, in the MOS capacitor geometry, in the particle sampling technique, and in the calibration procedures have resulted in the final design. We do not claim that the design has been optimized for every application; however, we consider the unit on which the report is based to be near an optimum design for detecting particles with a diameter between 2 and 10 microns.

Since the design of the particulate detector is to a large extent empirical, one can only conjecture about the design of a detector for particles greater than 10 microns and less than 2 microns. However, we are not aware of any fundamental reasons why a detector cannot be designed to operate outside the limits of 2 and 10 microns. The point is that for a detector to count particles with diameters from 2 to 10 microns, one should start with the unit described in this report. If the application is outside the 2 and 10 micron limits, from this report one can infer only a few factors pertinent to the design.

The major factors to consider when applying the results included in this report are:

(1) Geometric factors

- (a) The housing design should replicate the illustration in Figure 19. In particular, the dimensions of the particle accelerator tube and the nozzle to MOS sensor spacing should be maintained.
- (b) The MOS fabrication should follow the procedures in Section 5.0. Specifically, the aluminum thickness should be 500 Å and the SiO₂ thickness should be 700, 1000, or 1200 Å. Aluminum dot area and spacing are critical; however, some variation can be considered since calibration for efficiency will account for these variations.

(2) Particle Sampling

The volume of air sampled will depend upon the nozzle pressure as shown in Figure 11. The nozzle pressure must be adjusted to insure that the particle you wish to detect achieves sufficient velocity to initiate a discharge. For example, if a 9-micron particle is of interest, one finds in Figure 16 that the diamond microparticle has a mass of approximately 10^{-9} grams. From Figure 17, the threshold velocity for a 10^{-9} gram particle impacting a 700 Å oxide and 500 Å aluminum electrode is approximately 2,000 cm/sec. (This assumes a field of 2.2×10^6 volts/cm in the oxide.) In Figure 15, a particle velocity of 2,000 cm/sec can be achieved with a nozzle pressure of 0.95 atmospheres. Thus the vacuum line should be reduced below this level for reliable counting.

(3) Calibration

- (a) It has been inferred that particle hardness is important in the discharge process. To date most data have been obtained with alumina or diamond dust. For other dust environments, one should perform controlled laboratory tests with known (qualitatively) environments including the particles of interest.
- (b) The MOS capacitor may short after extended use. A shorting test such as a current or voltage measurement across the MOS unit should be included in the counting circuit. A threshold of acceptable performance can be established on the basis of d.c. or average values which would preclude the observation of the transient discharge.
- (c) The counting rate should be less than 10^3 counts per second. Even at this rate the MOS capacitors may degrade in a relatively short period of time. In most of this work we have considered 10 to 100 counts per second as acceptable counting rates which provide minutes to hours of continuous sampling without seriously degrading the response of the detector.
- (d) The threshold dependence on the voltage of the MOS capacitor will influence counting. One should be sure to use an applied voltage such that the field in the oxide is in excess of 2.2×10^6 volts/cm.
- (e) Counting efficiency will depend upon the ratio of the active (electrically connected) MOS capacitor area impacted to the total MOS area impacted. Although we find the factor of 4 (multiply counts by 4 to obtain actual count) to be a reasonable number for 15-mil dots on 20-mil centers, one should impact the sensor and then examine the impacted areas under a microscope to obtain assurance. Alignment errors can result in larger variations. One should remember that the entire area of the MOS array is the same order as the area of the nozzle outlet. Alignment must be carefully examined.

APPENDIX

GAS AND PARTICLE FLOW CHARACTERISTICS FOR SUCTION TYPE PARTICLE ACCELERATOR USED WITH MOS DETECTOR

By J. C. Mulligan

NOMENCLATURE

A	flow area
a	defined as intercept of linear velocity distribution in z
b	defined as slope of linear velocity distribution in z
C_1	defined as $18 \cdot \mu g/d^2 \cdot \rho_p$
C_p	specific heat at constant pressure
C_b	specific heat at constant volume
D	nozzle diameter
d	particle diameter
f	friction factor for tube flow (=0.02)
f_w	isentropic flow function (in $\sqrt{RT_o/g_c/AP_o}$)
g_c	gravitational constant ($32.2 \text{ lb}_m^{-\text{ft}}/\text{lb}_f^{-\text{sec}}^2$)
k	specific heat ratio (C_p/C_n)
K	particle to gas velocity ratio (V_p/V_g)
K_2	particle to gas velocity ratio in nozzle section
K_3	particle to gas velocity ratio in straight section
L_2	length of straight section
L_3	fictitious length necessary to achieve $M_e = 1.$
\dot{m}	mass flow rate
m_p	mass of particles per mass of gas ($\text{lb}_m \text{ particles}/\text{lb}_m \text{ gas}$)
M	Mach number
P	static pressure
P_{atm}	atmospheric pressure ($= P_i$)
Q	volume flow rate
R	gas constant
T	temperature
V	velocity
z	axial distance from inlet
Starred quantities - gas dynamics reference values	
e	density
u	absolute viscosity
u as unit	microns
<u>Subscripts</u>	
g	- gas
p	- particles
o	- stagnation state

Subscripts continued

i - inlet or stagnation conditions

e - exit

1 - upstream station

2 - throat station

3 - straight section exit station

I. INTRODUCTION

The analyses and computations presented here are concerned with the description of the flow characteristics of two vacuum type particle accelerators which have been used in a series of experiments utilizing an MOS type impactor for atmospheric particulate detection. The accelerators are essentially vacuum driven nozzles which accelerate sample air and particulates to a high velocity. The high velocity mixture is subsequently stagnated on the sensitive portion of the MOS impactor, at which point each of the particles generates a discharge which is ultimately counted in the MOS circuitry. In order to understand the important mechanisms occurring in the impaction process and to properly interpret the results of the experiments, it was necessary to know the actual velocities of the particles at impact under experimental conditions. The task of the work presented here, therefore, was to analyze the two types of nozzles which were used under vacuum conditions and to make estimates of the actual gas and particle velocities which were attained under experimental conditions.

Before gas dynamic type calculations could be carried out on the nozzles used in the experiments, it was necessary to investigate the accuracy which could be expected from a purely gas dynamic computation involving a particle laden gas. This was done and is the subject of section II, p. 60.

The first nozzle configuration used in the experiments was a converging nozzle, designed essentially to accelerate the gas-particle sample to a velocity sufficiently great to discharge the detector. A description of this device and some calculations of its characteristics is included in section III, p. 62.

It was realized that this rapid acceleration of the gas-particle mixture tended to accelerate the smaller particles more than the larger ones, thus tending to eliminate the larger particles role in detection. A combination of converging nozzle and straight tube was then used to provide a slower acceleration over a longer distance. This configuration tends to accelerate the larger particles significantly more. An analysis of the gas dynamic characteristics of this configuration is included in Section IV, p. 66, and a particle dynamics analysis is included in Section V, p. 70.

II. EFFECTS OF PARTICLES ON GAS DYNAMICS

The objective of the material presented here is to show that when particle concentrations are as low as they are in atmospheric air, gas velocities can be computed from gas dynamic computations by neglecting the presence of particles.

For internal flows, the conservation of mass of the gas phase is

$$\dot{m}_g = \rho_g V_g A \quad (1)$$

and the conservation of linear momentum for the composite medium is

$$\dot{m}_g \frac{dV_g}{dz} + \dot{m}_p \frac{dV_p}{dz} + A \frac{dP}{dz} = 0 \quad (2)$$

Assume that the ratio of the velocities of the particles and gas is K, i.e.

$$K = V_p / V_g = \text{const.} \quad (3)$$

This can be proven to be approximately true for nozzle flows (see ref. 1). Substituting equations (1) and (3) into equation (2) yields

$$\rho_g V_g \frac{dV_g}{dz} (1 + m_p K) + \frac{dP}{dz} = 0 \quad (4)$$

where m_p is (ρ_p / ρ_g) and ρ_p is the "partial" density of the particles. Thus, m_p is lb_m particles/lb_m gas. Now, this is the one-dimensional momentum equation of gas dynamics when

$$\rho'_g = \rho_g (1 + m_p K) \quad (5)$$

Also, $p_g = \rho_g R_g T = \rho'_g R'_g T / (H_m K) = \rho'_g R'_g T$ where

$$R'_g = R_g / (1 + m_p K) \quad (6)$$

Thus, it can be shown that if $K = \text{constant}$, the gas dynamic energy equation can be used in its homogeneous form when we replace unprimed by the following primed quantities:

$$C'_p = \frac{C_{pg} + m_p C_{pp} (T_o - T_p) / (T_o - T_g)}{1 + \frac{m_p}{p} K^2} \quad (7)$$

$$C'_b = C'_p - R' \quad (8)$$

$$K' = C'_p / C'_b \quad (9)$$

These primed quantities are known as "pseudo" properties in two phase flow theory. Equations (5) through (9) show that when m_p is small the flow characteristics of a nozzle are the same as if the particles were absent altogether, an assumption which is valid for the relatively dilute particulate concentrations in atmospheric air. Thus, particle sampler flows can be treated first from a gas dynamic point of view and secondly from a particle dynamic point of view. This is the computation approach which has been used here.

III. VACUUM NOZZLE CHARACTERISTICS

The purpose of the computations presented in this section was to first define the theoretical flow characteristics of the given nozzle and secondly to estimate actual gas velocities for the given nozzle with measured sampling rates. The computations make use of classical gas dynamic theory and procedures as presented in references 2,3,4. A description of the nozzle follows, along with the essentials of the computations.

The vacuum nozzle is a converging, conical nozzle with an inlet diameter of 0.225 inches, an exit diameter of 0.060 inches, and a 60° taper. A vacuum pump is used to establish a vacuum pressure at the exit area while the larger area is exposed to the sample gas at atmospheric pressure. The inlet area is assumed to be much larger than the exit area, the latter of which is 0.00283 in². The stagnation density at the entrance area is taken as 0.075 lb_m/ft³, the stagnation pressure at 14.7 psi and temperature of 70°F. The exit pressure, established by vacuum pump, and measured flow rates are as follows:

$$P_e = 13.5 \text{ in. Hg. Vac.}; 17.5 \text{ liter/min.}$$

$$P_e = 10 \text{ in. Hg. Vac.}; 16.2 \text{ liter/min.}$$

$$P_e = 2 \text{ in. Hg. Vac.}; 7.8 \text{ liter/min.}$$

A. Theoretical Flow Characteristics of Given Nozzle - In order to calculate the exit Mach number, M_e , the flow rate, Q , and the exit velocity, V_e , it was necessary to make the assumption that the nozzle behaves as an ideal (isentropic) expansion device from atmospheric conditions to the prescribed exit conditions. The pressure ratio P_e/P_i is first computed and M_e determined from gas dynamic tables. The quantity $\sqrt{RT_o/g_c}/AP_o$ is determined from Fig. 6-4 of reference 3, noting that $P_o = P_i$. The quantity $\sqrt{RT_o/g_c}/A_e P_o$ was computed to be 712.0 for the experimental conditions ($T_o - T_i$), and m subsequently calculated. The density ratio ρ/ρ_o was determined from the gas dynamic tables and ρ , Q and V

then calculated. Note that the Q evaluated at both inlet and exit conditions is given. A summary of the computations are shown in the following table.

P_e (in.Hg.Vac.)	P_e/P_i	M_e	$\dot{m}\sqrt{RT_o/g_C}/AP_i$	\dot{m}	ρ/ρ_o	ρ	Q_e	Q_i	V_e
13.5	0.549	0.97	0.68	$9.55(10)^{-4}$	0.65	.0487	33.3	21.5	998
10	0.666	0.785	0.65	$9.13(10)^{-4}$	0.75	.0562	27.5	20.6	823
2	0.933	0.315	0.34	$4.77(10)^{-4}$	0.95	.0712	11.4	10.8	341

The flow rates, Q are given in liter/min, the mass flow rate \dot{m} is lb_m/sec and the exit velocity given in ft/sec. The flow rate Q_i should correspond to the experimentally determined sampling rate. A plot of Q_i and V_e versus P_e/P_i is shown in Figure A-1. Comparing the Q_i (liters/min.) with the measured values, it is seen that the theoretically predicted flow rate is approximately 25% larger than measured. This was expected since inefficiencies in a simple nozzle such as that used in the experiments are normally of this order.

B. Actual Velocities of Given Nozzle for Measured Flow Rates - The actual velocities at the nozzle exit section which correspond to actual measured inlet flow rates were computed. From the measured Q and the inlet density, \dot{m} is computed. From this \dot{m} and again the inlet conditions, the flow function $\dot{m}\sqrt{RT_o/g_C}/A_e P_o$ is computed. This function is tabulated in reference 4 versus M_e . Thus, with this M_e the Q_e can be determined from ρ/ρ_o and thus V_e . Note that this procedure does not require an isentropic computation and therefore if Q_i is actual, then V_e should be a good estimate. A tabulation of some computations are as follows.

Q_i	\dot{m}	$\dot{m}\sqrt{RT_o/g_C}/AP_o$	M_e	e/e_o	Q_e	V_e
17.5	$7.75(10)^{-4}$	0.552	0.56	0.86	0.012	610
16.2	$7.18(10)^{-4}$	0.511	0.50	0.885	0.0108	550
7.8	$3.45(10)^{-4}$	0.246	0.21	0.978	0.0047	239

The flow rate Q_i is in liters/min, \dot{m} in lb_m/sec , Q_e in ft^3/sec and V_e in ft/sec . Note that the actual exit velocity is only about 60% of that predicted theoretically, again an expected result. A plot of the actual Q_i and V_e are also included in Figure A-1.

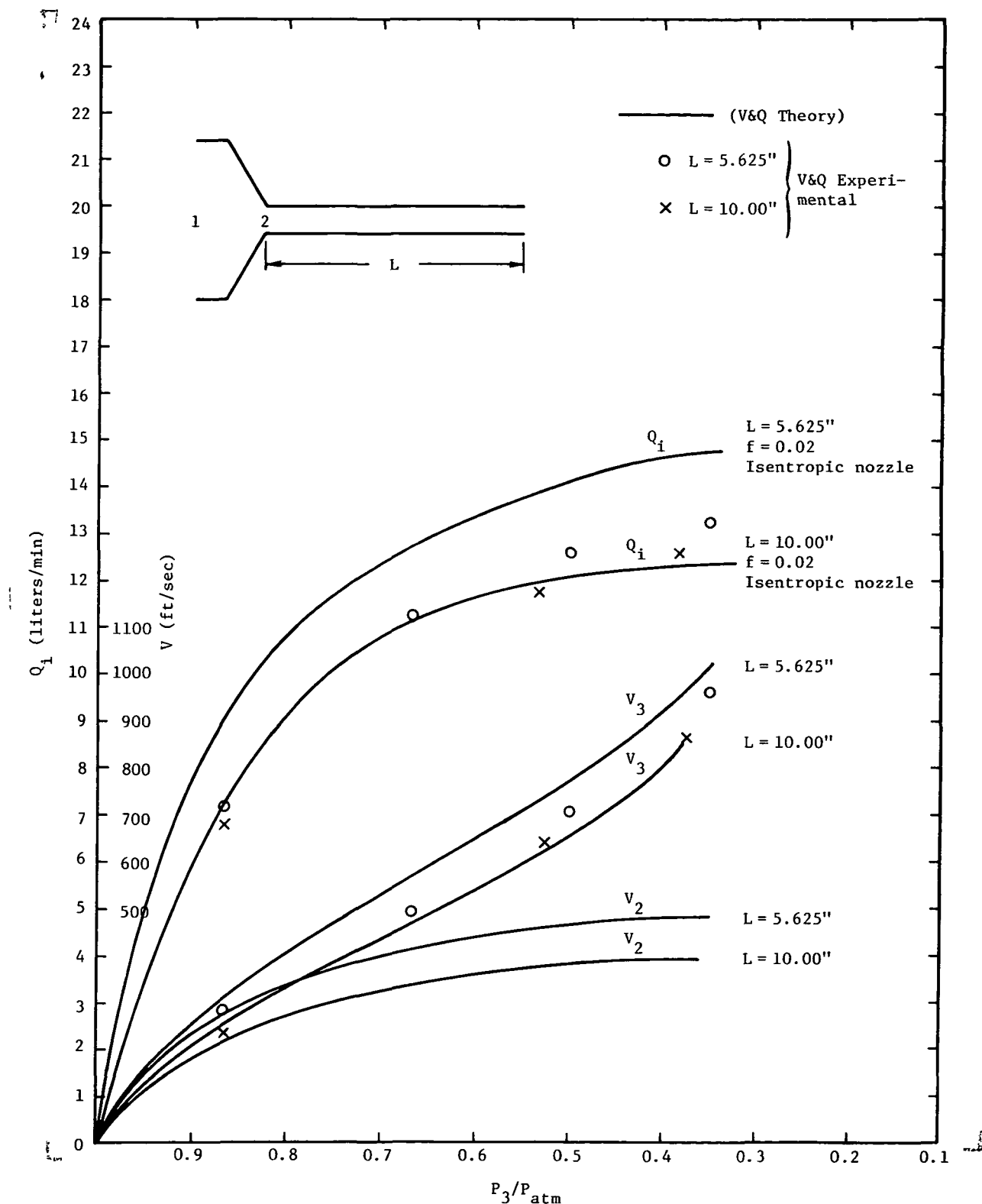


Figure A-1. Nozzle Flow and Velocity versus Nozzle Pressure.

IV. CHARACTERISTICS OF NOZZLE AND STRAIGHT TUBE COMBINATION

It has been recognized that even though a simple converging nozzle is sufficient to accelerate the gas, it may not provide a long enough flow path to allow time for the acceleration of entrained particles. Thus, it was thought that an additional length of straight tube attached to the exit of a converging nozzle would facilitate the acceleration of a greater percentage of the larger particles. A sketch of this configuration is shown in Figure A-2. The nozzle exit, Station 2, and the straight tube were of an 0.062 in inside diameter. Two lengths were used in the experiments, 5.625 inch and a 10.0 inch section. Again, the nozzle inlet diameter was large in comparison with the throat diameter. As before, a theoretical analysis of this nozzle configuration and computations of actual characteristics were carried out. A summary of some experimental data is as follows:

<u>$L_2 = 10.0 \text{ in.}$</u>			<u>$L_2 = 5.625 \text{ in.}$</u>		
<u>P_e</u>	<u>P_e/P_i</u>	<u>Q_i</u>	<u>P_e</u>	<u>P_e/P_i</u>	<u>Q_i</u>
18.5	0.382	12.6	19.5	0.35	13.25
14	0.533	11.8	15	0.50	12.6
4	0.867	6.8	10	0.666	11.1
			4	0.867	7.2

P_e is in inches of Hg., and Q_i in liters/min. sampled.

A. Theoretical Flow Characteristics of Given Combination - Assuming isentropic flow in the nozzle section and friction flow in the straight section, the computation procedure is of a trial-and-error nature. The Mach number at the exit station, 3, M_3 is first assumed and the friction length fL_3/D read from the Fanno tables of reference 4. The actual friction length fL_2/D is then computed and added to fL_3/D to form the friction length corresponding to station 2, $f(L_3+L_2)/D$. Then M_2 is read from the Fanno tables for this friction length, along with P_2/p^* . Since M_3 is known, P_2/P_3 can be calculated from $(\frac{P_2}{P^*})/(\frac{P_3}{P^*})$ and P_2/P_{atm} calculated from $(\frac{P_2}{P_3})(\frac{P_3}{P_{atm}})$.

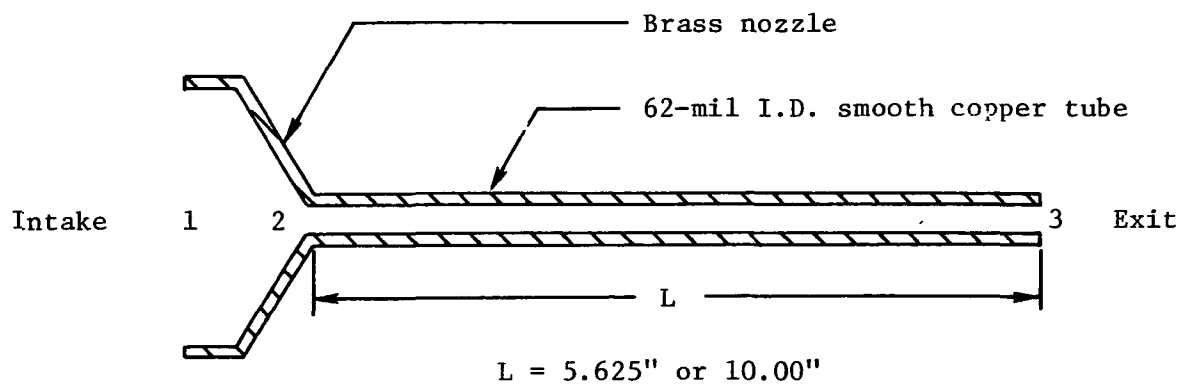


Figure A-2. Nozzle and Straight Tube Combination.

From P_2/P_{atm} , M_2 is determined from the isentropic tables and compared with the previously computed M_2 . Using this procedure, the following data was generated. Noting also that $\dot{m} = AP_o f_w / \sqrt{RT_o} / g_C = f_w / 712$ and the flow function f_w is read from the isentropic tables of reference 4 for each M_2 .

Case	P_3/P_{atm}	L_2	fL_2/D	M_3	M_2	P_2/P_3	P_2/P_{atm}	f_w	$\dot{m}(10)^3$	Q_i
1	0.35	5.625	1.82	1.0	0.43	2.50	0.875	0.464	0.652	14.8
2	0.50	5.625	1.82	0.72	0.42	1.77	0.885	0.448	0.63	14.2
3	0.666	5.625	1.82	0.51	0.375	1.38	0.913	0.404	0.566	12.8
4	0.867	5.625	1.82	0.23	0.254	1.10	0.956	0.29	0.407	9.18
5	0.382	10.00	3.24	0.81	0.354	2.40	0.916	0.39	0.548	12.4
6	0.867	10.00	3.24	0.57	0.336	1.73	0.920	0.376	0.528	12.0
7	0.867	10.00	3.24	0.23	0.205	1.12	0.975	0.231	0.325	7.35

In the above tabulation, \dot{m} is in lb_m/sec and $Q_i = \dot{m}/0.075$ is converted to liters/min. Some additional computations of velocities were made and are tabulated below:

Case	Q_1	ρ_2/ρ_{atm}	Q_2	V_2	V_2/V^*	M_3	V_3/V^*	V_3/V_2	V_3
1	$.87(10)^{-2}$.9094	$.958(10)^{-2}$	487	.4729	1.0	1.0	2.11	1030
2	$.84(10^{-2})$.9170	$.916(10)^{-2}$	467	.4522	.72	.7508	1.66	775
3	$.755(10)^{-2}$.9347	$.808(10)^{-2}$	411	.3999	.51	.5447	1.36	560
4	$.542(10)^{-2}$.968	$.56(10)^{-2}$	285	.2770	.28	.3043	1.10	314
5	$.73(10)^{-2}$.9395	$.777(10)^{-2}$	396	.3830	.81	.8343	2.18	863
6	$.705(10)^{-2}$.9445	$.747(10)^{-2}$	380	.3682	.57	.6051	1.64	623
7	$.433(10)^{-2}$.9803	$.442(10)^{-2}$	225	.2182	.23	.2506	1.15	259

In this table Q_1 and Q_2 are flow rates evaluated at stations 1 and 2 respectively in ft^3/sec . The density ratio was taken from the isentropic tables at M_2 and V_2 computed from Q_2/A_2 . The velocity ratios with the starred reference velocities were taken from the Fanno tables at M_2 and M_3 and V_3 subsequently calculated in ft/sec. In all of the computations, a friction factor f of 0.02 was used and checked against Reynolds number as being representative. The results of the computations are illustrated in Figure A-1.

B. Actual Velocities of Given Combination with Measured Flow Rates

The computations presented here are the results of the calculations of the actual exit velocities for certain measured flow rates. As above, a trial-and-error procedure is necessary. The governing equations are

$$f_w \frac{(P_{atm}/P_3)}{\sqrt{k}} = M_3 (1 + \frac{k-1}{2} M_3^2)^{1/2} \quad (10)$$

$$V_3 = M_3 (1 + \frac{k-1}{2} M_3^2)^{-1/2} \sqrt{kg_c RT_1} \quad (11)$$

and

$$f_w = \dot{m}(712) \quad (12)$$

From a measured Q_1 and a known ρ_1 , \dot{m} is determined and subsequently f_w . Then, $f_w (P_{atm}/P_3)/\sqrt{k}$ is computed from measured pressures and M_3 determined from equation (10) by trial-and-error. Subsequently, V_3 is computed from equation (11). A summary of the computations are included in the following table.

Case	\dot{m}	$f_w \frac{(P_{atm}/P_3)}{\sqrt{k}}$	M_3	V_3
1	$.587(10)^{-3}$	1.0	.92	960
2	$.558(10)^{-3}$	0.672	.65	705
3	$.491(10)^{-3}$	0.443	.44	487
4	$.369(10)^{-3}$	0.256	.25	280
5	$.557(10)^{-3}$	0.879	.82	869
6	$.552(10)^{-3}$	0.623	.60	654
7	$.301(10)^{-3}$	0.209	.21	235

In this table \dot{m} is in $lb_m/\text{sec.}$ and V_3 in $ft/\text{sec.}$ These values are shown plotted in Figure A-2 along with the theoretical results. The experimental Q_1 is lower than the theoretical for $L_2 = 5.625$ in. but in essential agreement for $L_2 = 10.00$ in. This is also true for the V_3 plot. This is believed due to the reduction of losses in the nozzle reaction which occur when the velocities in the nozzle section are reduced by adding additional length on the straight section. Computed values of V_2 were not included as they can be adequately estimated from theoretical values shown.

V. PARTICLE VELOCITIES IN NOZZLE AND STRAIGHT TUBE COMBINATION

It can be shown (see reference 1, p. 211) that the ratio of particle to gas velocity in a duct is a constant when the axial variation of the gas velocity is linear. That is,

$$\frac{v_p}{v_g} = K = \text{constant} \quad (13)$$

when $v_g = a + bz$ where z is axial distance from duct inlet. This result, of course, is valid for low particle Reynolds numbers and Stokesian drag. The velocity distribution in z in nozzle and straight duct flows is here approximated to be linear. Although this isn't entirely correct, it is a good approximation for most nozzles and ducts and especially for the problem under consideration here. Thus,

$$v_p = KV_g \quad (14)$$

and

$$v_p = C_1 \int_{z_1}^z \frac{1-K}{K} dz + v_p(z_1)$$

$$v_p = C_1 \frac{(1-K)}{K} (z-z_1) + v_p(z_1) \quad (15)$$

Equation (15) is developed from the particle momentum equation incorporating Stokes drag law. $C_1 = 18 \cdot \mu_g / d^2 \cdot \rho_p$ where d is the particle diameter.

A. Entrance Nozzle ($K = K_2$)

$$v_p = C_1 \frac{(1-K_2)}{K_2} z + v_p(z=0) \quad (16)$$

where $v_p(z=0) = 0$ and $v_p = K_2 \cdot v_g$. Now, using this latter ratio

$$v_g = C_1 \frac{(1-K_2)}{K_2} z + \frac{v_p(0)}{K_2} = C_1 \frac{(1-K_2)}{K_2} \cdot z + v_g(0) \quad (17)$$

Now, assuming $V_g = V_g(0) + bz$, it can be seen that

$$b = \frac{C_1(1-K_2)}{K_2^2}$$

or, taking the positive root,

$$K_2 = \frac{-C_1 + \sqrt{C_1^2 + 4bC_1}}{2b} \quad (18)$$

and

$$b = \frac{V_g - V_g(0)}{z-0} \quad (19)$$

Knowing V_{g2} and z_2 , b can be determined and thus K_2 . From K_2 , then V_p can be calculated. From the entrance nozzle $V_g(0) = 0$ and $V_p(0) = 0$. Thus, $b = V_{g2}/z_2$ and $V_p = K_2 \frac{C_1(1-K_2)}{K_2^2} z$.

Thus,

$$V_p = C_1 \frac{(1-K_2)}{K_2} \cdot z \quad (20)$$

where $C_1 \approx 18 \text{ } \mu\text{g}/d^2 \rho_p$ and $z_2 \approx 3/32 \text{ in.} = 0.0078 \text{ ft.}$

Computations were made for three particle sizes. These, along with some property data are listed below.

$$\begin{aligned} d &= 3\mu = 1.18(10)^{-4} \text{ in.} \\ &= 9\mu = 3.55(10)^{-4} \text{ in.} \\ &= 15\mu = 5.91(10)^{-4} \text{ in.} \\ \rho_p &= 2.5(62.4) = 210 \text{ lb}_m/\text{ft}^3 \\ \mu_{air} &= 0.042 \text{ lb}_m/\text{hr.ft.} \\ C_1 &= 1.38(10)^{-4}/d^2 \text{ sec}^{-1} \end{aligned}$$

d	$1.18(10)^{-4}$	$2.36(10)^{-4}$	$3.55(10)^{-4}$	$5.91(10)^{-4}$	in. sec^{-1}
C_1	$0.993(10)^4$	$.248(10)^4$	$.1095(10)^4$	$0.0395(10)^4$	

The computations are summarized in section C, p. 73.

B. Straight Tube ($K=K_3$)

A similar type of analysis is carried out for the straight tube. However, K_3 for the tube is larger in magnitude than K_2 for the nozzle. Thus, at station 2 v_p can have two values depending on the value of K used to compute it. A correction is applied to avoid this difficulty. The particle velocity is given by

$$v_p = C_1 \frac{(1-K_3)}{K_3} (z-z_2) + v_p(z_2) \quad (21)$$

and the gas velocity by

$$v_g = C_1 \frac{(1-K_3)}{K_3^2} (z-z_2) + v_p(z_2)/K_3 \quad (22)$$

Again $v_g = v_g(z_2) + b(z-z_2)$ where $b = (v_{g3}-v_{g2})/(z_3-z_2)$. Thus,

$$v_g(z_2) + b(z-z_2) = C_1 \frac{(1-K_3)}{K_3^2} (z-z_2) + v_p(z_2)/K_3. \quad (23)$$

Now, if $v_g(z_2)$ is placed equal to $v_p(z_2)/K_3$ then as before

$$bK_3 = C_1 \frac{(1-K_3)}{K_3}$$

This however would produce a $v_p(z_2)$ which is too large because K_3 is larger than K_2 . Also, $v_p(z_3)$ would be too large by the same amount because the distribution is linear. Fortunately, this excess in v_p in the straight section is known and can be subtracted from the final result. Thus

$$v_{p3} = K_3 \cdot v_{g3} - (K_3 - K_2) v_{g2} \quad (24)$$

where $b_3 = (v_{g3}-v_{g2})/(z_3-z_2)$ and

$$K_3 = \frac{-C_1 + \sqrt{C_1^2 + 4b_3 C_1}}{2b_3} \quad (25)$$

The straight tube computations are also summarized in the following section.

C. Computations of Particle Velocities

The following is a summary of the computations outlined in sections A and B.

d=3μ

<u>P₃/P_i</u>	<u>V₂</u>	<u>V₃</u>	<u>(z₂-0)</u>	<u>(z₃-z₂)</u>	<u>b₃</u>	<u>b₂</u>	<u>C₁</u>	<u>K₃</u>	<u>K₂</u>	<u>V_{P2}</u>	<u>V_{P3}</u>
0.35	480	960	0.094	5.625	1025	$6.12(10)^4$	$.993(10)^4$.912	.33	157	596
0.50	450	705	0.094	5.625	545	$5.75(10)^4$	$.993(10)^4$.945	.338	152	392
0.666	375	487	0.094	5.625	239	$4.80(10)^4$	$.993(10)^4$.985	.364	136	245
0.867	260	280	0.094	5.625	42.5	$3.32(10)^4$	$.993(10)^4$	1.0	.417	109	128
0.382	400	869	0.094	10.00	563	$5.1(10)^4$	$.993(10)^4$.942	.354	141	585
0.533	380	654	0.094	10.00	329	$4.85(10)^4$	$.993(10)^4$.973	.362	137	404
0.867	200	235	0.094	10.00	42	$2.55(10)^4$	$.993(10)^4$	1.0	.47	88	129
						•					

d=9μ

<u>P₃/P_i</u>	<u>C₁</u>	<u>K₃</u>	<u>K₂</u>	<u>V_{P2}</u>	<u>V_{P3}</u>	<u>C₁</u>	<u>K₃</u>	<u>K₂</u>	<u>V_{P2}</u>	<u>V_{P3}</u>
.35	$.1095(10)^4$.63	.125	60	363	$3.95(10)^2$.454	.0771	37	255
.50	$.1095(10)^4$.732	.129	57.8	244	$3.95(10)^2$.56	.0795	35.7	179
.666	$.1095(10)^4$.837	.14	52.5	147	$3.95(10)^2$.693	.0867	32.5	110
.867	$.1095(10)^4$.954	.167	43.5	62	$3.95(10)^2$.856	.103	26.8	0
.382	$.1095(10)^4$.728	.146	58.4	399	$3.95(10)^2$.554	.0842	33.7	294
.533	$.1095(10)^4$.807	.142	53.9	274	$3.95(10)^2$.641	.0862	32.7	208
.867	$.1095(10)^4$.893	.188	37.6	79	$3.95(10)^2$.845	.117	23.4	52

In the above tabulation V_2 and V_3 are the gas velocities in ft/sec., the z's are in inches, b_3 and b_2 in sec⁻¹, C_1 in sec⁻¹ and the particle velocities in ft/sec. These latter quantities were computed by means of equations (24) and (20) and are plotted in Figure A-3.

The accuracy of the above calculations is difficult to assess. Predicting particle entrainment in gas streams is a difficult problem. It is believed that the above computations at least establish a lower bound for the exit particle velocities. In all probability, the actual velocities will be of the order of the above estimates or slightly greater. The scheme used in the above computations should at least be accurate than a prediction based on a constant, average gas velocity, a computation which might be considered

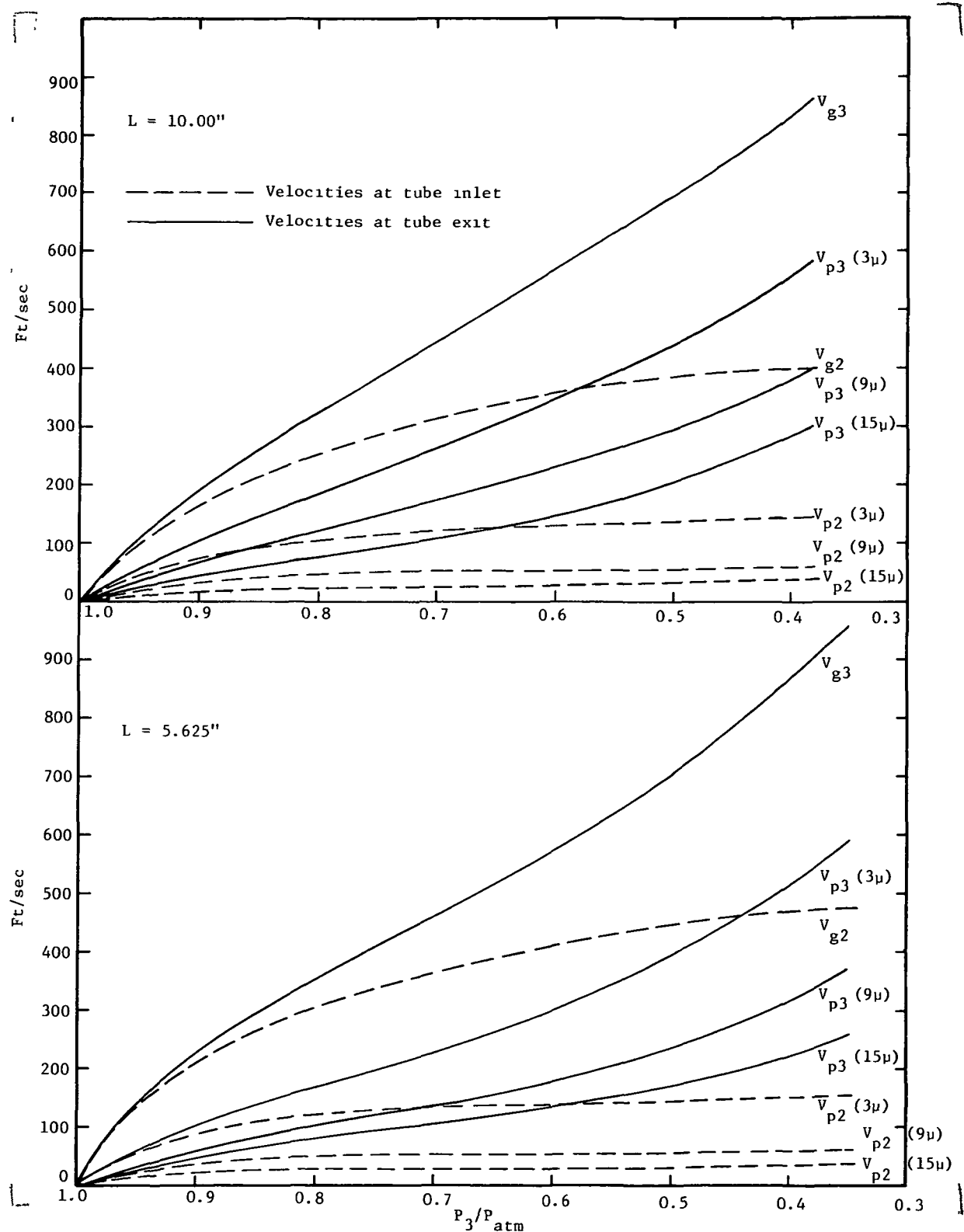


Figure A-3. Particle Velocities as Functions of Nozzle Pressure.

a first estimate procedure. A more sophisticated procedure than that used above for making the computations is certainly not evident.

REFERENCES

1. Wallis, G. B., One-Dimensional Two-Phase Flow, McGraw-Hill, 1969.
2. Shapiro, A. H., The dynamics and Thermodynamics of Compressible Fluid Flow, Vol. 1, Ronald Press, 1953.
3. Owczarek, J. A., Fundamentals of Gas Dynamics, International Textbook Co., 1964.
4. Rotty, R. M., Introduction to Gas Dynamics, John Wiley, 1962.